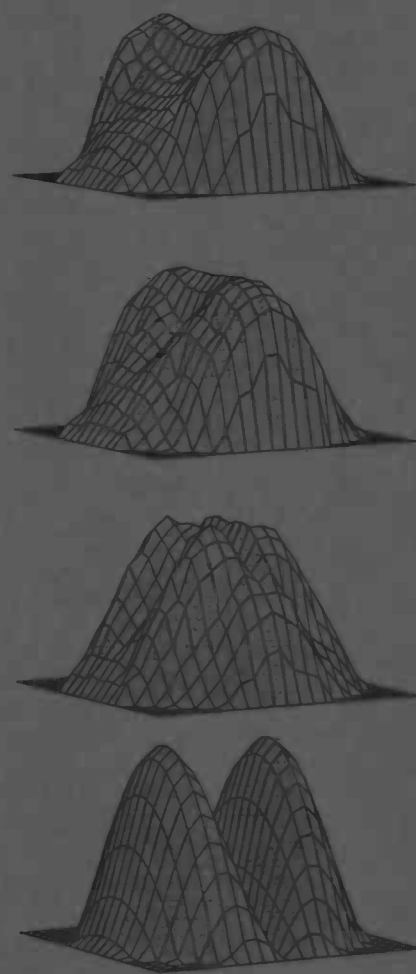




Numerical simulation of a three dimensional, pulsating flow in the basilar artery

Sander van der Meulen



Rijksuniversiteit Groningen
Bibliotheek
Wiskunde / Informatica / Rekencentrum
Landleven 5
Postbus 800
9700 AV Groningen

Vakgroep
Wiskunde

WORDT
NIET UITGELEEND

RuG



Master's thesis

Numerical simulation of a three dimensional, pulsating flow in the basilar artery

Sander van der Meulen

Rijksuniversiteit Groningen
Vakgroep Wiskunde
Postbus 800
9700 AV Groningen

August 1996

Preface

This report is the result of the work done for my engineering degree research project at the Department of Mathematics at the University of Groningen. I would like to thank prof. dr. ir. H.W. Hoogstraten for his supervision during this year. With his guidance I was able to write this report. I would also like to thank D.D. de Vries en drs. K. Visser for their support when the computers did not do what I wanted.

Furthermore I would like to thank everyone on IWI 227. With their cups of coffee, suggestions and useful tips it was a great pleasure to work there. I am especially very thankful to Wilhard. His advices and peptalks were absolutely 'top'.

At last I would like to thank Brigitte. She knows why.

I hope the reader will enjoy reading this report.

Sander van der Meulen
Groningen, August 1996

Editorial

The primary goal of ergonomics is to move away from static, stiff postures and to develop a more dynamic way of working. This is not always easy, particularly when it comes to the design of workstations and workplaces. However, research has shown that such changes can lead to significant improvements in both physical and mental health.

One such area of concern is the use of mobile computing devices, such as laptops. These have been found to be associated with increased levels of physical strain and discomfort, particularly when used for extended periods of time. In response to this, researchers have developed a range of interventions aimed at reducing the negative effects of laptop use. These include the use of external keyboards and mice, as well as the development of specialized laptop stands and chairs.

Mobile computing devices
and their impact on health

Edited by Michael J. Haines and Mark A. Williams

Department of Psychology, University of Exeter, UK

Accepted: 10 August 2009; first published online: 10 September 2009

© 2009 Taylor & Francis
ISSN: 0014-0139 print/1366-5847 online
DOI: 10.1080/00140139.2009.403922
http://www.informaworld.com

Published online in *Ergonomics* at <http://www.informaworld.com> on 10 September 2009

10.1080/00140139.2009.403922

Downloaded At: 10/29/2009 10:45:20 AM

Copyright © Taylor & Francis
1366-5847/09/101366-01\$15.00
http://www.informaworld.com

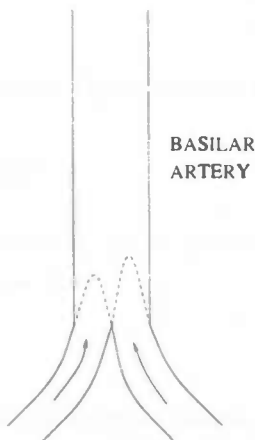
Contents

1	Introduction	5
2	Mathematical model	7
2.1	Introduction	7
2.2	The Navier-Stokes equations	7
2.3	Womersley profile	8
2.4	The finite-element grid	9
3	Numerical model	11
3.1	Introduction	11
3.2	Basis functions and elements	11
3.3	The Ritz-method	13
3.4	The Galerkin method	14
3.5	The penalty function method	15
3.6	Time integration	15
3.7	The linearizations	16
3.7.1	Picard linearization	17
3.7.2	Newton iteration	17
3.8	Initial and boundary conditions	18
3.9	Matrix decomposition	19
4	Results	21
4.1	Stationary flow	21
4.2	Instationary flow	24
4.2.1	Womersley profile	27
4.3	Computations with a secondary velocity field	28
4.3.1	Stationary flow	29
4.3.2	Instationary flow	29
4.3.3	The pulses of the heart	30
5	Figures	33
6	Discussion, conclusions and recommendations	69

Chapter 1

Introduction

The flow of blood in arteries has been simulated numerically before. Most of the times it concerned a steady flow or an axi-symmetrical, unsteady flow that could be computed on a two-dimensional grid. Now, it was the question to compute a three-dimensional, unsteady flow and to examine what was possible on the computers of our mathematics department. The reason for being that interested in the possibilities for computing a three-dimensional, instationary flow is that one wants to get insight in the flow phenomena in the basilar artery, an important input blood vessel for the cerebro-vascular circulation. The basilar artery arises from the union of the vertebral arteries and is located at the base of the brain. It has a diameter of about 3 mm and a length of 30-50 mm. At its end, the artery divides into both posterior cerebral arteries, which are part of the circle of Willis, an arterial network from which six cerebral arteries distribute the blood to various parts of the brain.



There are two main reasons to study the flow phenomena in the basilar artery. First, the length of the basilar artery is relatively small . It is very likely that the flow is not fully developed at the end of the artery, where it divides into two arteries. It is known that the

flow in the circle of Willis is very sensitive to small disturbances. So, it is important to know what happens at the end of the basilar artery. Second, it is known from anatomical research that the basilar artery is often affected by atherosclerosis and it is assumed that flow phenomena play an important role in the occurrence of atherosclerosis. There is evidence that atherosclerosis lesions concentrate in regions of low wall shear stress and recirculation. It is therefore important to look at recirculation regions.

In this study we consider a three-dimensional, pulsating flow of a Newtonian fluid in a straight, circular tube with rigid walls. To model this flow on the computer system of the department, we want to make this tube as long as was possible. The computations are done with the finite element method package SEPRAN. The limitations of the computations on the computers CIWI4¹ and CIWI10² are given by the required computer memory space. Soon it was clear that we could not make the tube as long as we wanted. That is the reason why we examined whether it was possible to place some tubes behind each other. Then it was possible to compute the flow in each tube separately, which saved a lot of computer memory space and computation time.

This principle was examined for both a stationary flow and an instationary flow in order to get insight in the error that was made. After knowing the error we computed an instationary flow that was like a flow in the basilar artery.

¹CIWI4: HP9000/735. Internal memory: 400MB. Velocity: 40 Megaflop

²CIWI10: HP9000/755. Internal memory: 512MB. Velocity: 40 Megaflop

Chapter 2

Mathematical model

2.1 Introduction

Consider an unsteady, three-dimensional flow of an incompressible Newtonian fluid in a semi-infinite, straight, circular tube. The flow is described by the Navier-Stokes equations, which are given in section 2.2. The correctness of the numerical results can be checked by comparing the results with the Womersley theory. In section 2.3 this theory is explained. In section 2.4 the modelling of the region is discussed.

2.2 The Navier-Stokes equations

An unsteady flow of an incompressible, Newtonian fluid is described by the Navier-Stokes equations. These equations are given by the conservation of mass (continuity equation):

$$\nabla \cdot \vec{v} = 0 \quad (2.1)$$

and by the conservation of momentum (momentum equation):

$$\rho \frac{\partial \vec{v}}{\partial t} + \rho(\vec{v} \cdot \nabla) \vec{v} = -\nabla p + \mu \Delta \vec{v} \quad (2.2)$$

with ρ the density, \vec{v} the velocity vector, p the pressure and μ the dynamical viscosity. In a steady flow equation (2.2) reduces to :

$$\rho(\vec{v} \cdot \nabla) \vec{v} = -\nabla p + \mu \Delta \vec{v} \quad (2.3)$$

Furthermore the Reynolds number Re is introduced. It is defined by:

$$Re = \frac{\rho d \hat{v}}{\mu} \quad (2.4)$$

with d the diameter of the tube and \hat{v} the time-averaged cross-sectional mean velocity in axial direction.

2.3 Womersley profile

When a pulsating entry flow in a tube of radius R is considered, the flow will become fully developed at the end of the tube. It is then possible to compute the velocity analytically. One therefore needs the axi-symmetric Navier-Stokes equations. These are given by:

$$\rho \frac{\partial u}{\partial t} + \rho(u \frac{\partial u}{\partial r} + w \frac{\partial u}{\partial z}) = -\frac{\partial p}{\partial r} + \mu(\frac{\partial^2 u}{\partial r^2} + \frac{1}{r} \frac{\partial u}{\partial r} + \frac{\partial^2 u}{\partial z^2} - \frac{u}{r^2}) \quad (2.5)$$

$$\rho \frac{\partial w}{\partial t} + \rho(u \frac{\partial w}{\partial r} + w \frac{\partial w}{\partial z}) = -\frac{\partial p}{\partial z} + \mu(\frac{\partial^2 w}{\partial r^2} + \frac{1}{r} \frac{\partial w}{\partial r} + \frac{\partial^2 w}{\partial z^2}) \quad (2.6)$$

with r the radial coordinate, z the axial coordinate, u the velocity in radial direction and w the velocity in axial direction. As $z \rightarrow \infty$, $u = 0$ and $\frac{\partial w}{\partial z} = 0$. This leads to the following equations:

$$0 = -\frac{\partial p}{\partial r} \quad (2.7)$$

$$\rho \frac{\partial w}{\partial t} = -\frac{\partial p}{\partial z} + \mu(\frac{\partial^2 w}{\partial r^2} + \frac{1}{r} \frac{\partial w}{\partial r}) \quad (2.8)$$

From equation (2.7) it follows that the pressure is constant in radial direction. So it can be stated that $\frac{\partial p}{\partial z} = p_0 e^{i\omega t}$ (with $p_0 < 0$) and $w(r, z, t) = A(r)e^{i\omega t}$. Substitute this in (2.8) and the equation is transformed to:

$$i\omega \rho A = -p_0 + \mu(A_{rr} + \frac{1}{r} A_r) \quad (2.9)$$

This is equivalent with (recalling that $-1 = i^2$)

$$A_{rr} + \frac{1}{r} A_r + \frac{i^3 \omega \rho}{\mu} A = \frac{p_0}{\mu} \quad (2.10)$$

With the transformation $x = \sqrt{\frac{i^3 \omega \rho}{\mu}} r$ the homogeneous version of equation (2.10) reads:

$$A_{xx} + \frac{1}{x} A_x + A = 0 \quad (2.11)$$

which is the well-known Bessel equation of order zero and which has the solution

$$\begin{aligned} A &= \alpha J_0(x) + \beta Y_0(x) \\ &= \alpha J_0(x) + \beta (J_0(x) \log x + \frac{x^2}{4} - \frac{3x^4}{128} + \dots) \end{aligned} \quad (2.12)$$

For $x = 0$, Y_0 is not defined. Therefore $\beta = 0$. The solution of (2.10) reads

$$A = \frac{-p_0}{i\omega \rho} + c_1 J_0\left(\frac{i^{\frac{3}{2}} \omega^{\frac{1}{2}} \rho^{\frac{1}{2}}}{\mu^{\frac{1}{2}}} r\right) \quad (2.13)$$

Of course there is a boundary condition : $A(R) = 0$, implying that the velocity on the wall is equal to zero. This gives

$$A = \frac{-p_0}{i\omega\rho} \left(1 - \frac{J_0\left(\frac{i^{\frac{3}{2}} \omega^{\frac{1}{2}} \rho^{\frac{1}{2}}}{\mu^{\frac{1}{2}}} r\right)}{J_0\left(\frac{i^{\frac{3}{2}} \omega^{\frac{1}{2}} \rho^{\frac{1}{2}}}{\mu^{\frac{1}{2}}} R\right)} \right) \quad (2.14)$$

Then $w = Ae^{i\omega t}$ and because this is in complex form, one needs to take the real part.

$$w = \operatorname{Re} \left(\frac{-p_0}{i\omega\rho} \left(1 - \frac{J_0\left(\frac{i^{\frac{3}{2}} \omega^{\frac{1}{2}} \rho^{\frac{1}{2}}}{\mu^{\frac{1}{2}}} r\right)}{J_0\left(\frac{i^{\frac{3}{2}} \omega^{\frac{1}{2}} \rho^{\frac{1}{2}}}{\mu^{\frac{1}{2}}} R\right)} \right) e^{i\omega t} \right) \quad (2.15)$$

This is the contribution to the velocity due to the oscillation, which should be added to the stationary flow. The stationary flow can be computed from equation (2.9) when the frequency of the oscillation is zero ($\omega = 0$). The total velocity in axial direction is then given by:

$$w_{\text{flow}} = \frac{-p_0 R^2}{4\mu} \left(1 - \frac{r^2}{R^2} \right) + w \quad (2.16)$$

This solution can be used to check the correctness of the computer program and the accuracy of the solution, by comparing the numerical solution far downstream with equation (2.16). Therefore one needs to know the value of p_0 . This parameter p_0 can be computed by the fact that the flux at the inflow surface is equal to the flux at the outflow surface, for every t . The flux at the outflow surface can be computed by integrating w_{flow} over this surface. This integral contains the parameter p_0 . The flux at the inflow surface is computed by integrating the prescribed velocity at the inflow surface.

2.4 The finite-element grid

For the numerical solution of the equations (2.1) and (2.2) a computational grid is to be constructed. Because the region is semi-infinite, it is impossible to work with a finite number of elements. The semi-infinite region is made finite by cutting off the region at a large distance from the entrance. The cut can be justified because the velocity \vec{v} goes asymptotically to the velocity given by (2.16), under the condition $\frac{\partial}{\partial z} = 0$. The error that is made in this way has some effect on the numerical solution in the neighbourhood of the outflow plane. The error further away from the outflow plane is much smaller than the error made by the numerical computation. For the computations in one solid tube a mesh like in figure 2.1 has been used. Because the flow development in the axial direction is faster near the inflow boundary than far downstream, where the flow is almost fully developed, gridlines have to be concentrated near the entrance. It was possible to make the grid longer in case of a steady flow than in case of an unsteady flow, because the required memory space is less in case of a steady flow.

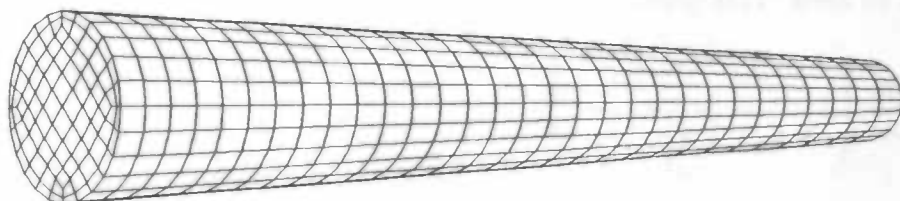


Figure 2.1: mesh for one tube with length 10 times the diameter

For the computation of the flow in several tubes, the following principle was used. An inner surface was created one element before the end of the tube. When the computations for tube 1 were ready, the values of the velocity at this inner surface were transferred to the surface at the front of tube 2. Then the computation started again, of course with the values of the outflow of tube 1 as inflow for tube 2. This principle could be repeated as often as wanted. The advantage of this principle is that the required memory space was less than the memory used for the computations in one large tube, and that the computation time was shorter. The reason for creating an inner surface one element before the end of the tube, is that there is made a numerical error at the end of the tube. In this way one prevents transferring this error to the next tube. In case of an instationary flow the time was increased with δt after computing the flow in each tube. Of course, a cross-section of these tubes is equal to a cross-section of one large tube.

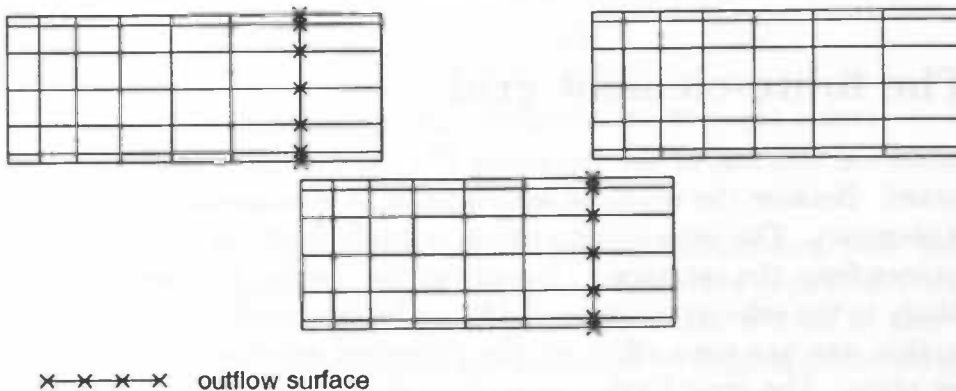


Figure 2.2: principle for computing the flow in several tubes

Chapter 3

Numerical model

3.1 Introduction

In order to be able to solve the Navier-Stokes equations numerically, one must define where the flow is computed. As can be seen in section 2.4 the region is divided in small subregions. On all those subregions one has to construct so-called basis functions to build up the matrices. In section 3.2 is explained how these basis functions can be constructed. Once having the matrices for the Navier-Stokes equations discretization and linearization must be applied. For the linearization of the non-linear terms, two techniques are available for SEPRAN (see section 3.7):

- Picard linearization
- Newton iteration

For the discretization Galerkin has been used (see section 3.4). The system of equations that arises, can be reduced using the penalty function method (section 3.5). This method saves a lot of computing time and computer memory. In section 3.6 the treatment of the time derivative is explained. Finally, in section 3.9, the actual solving of the set of equations is carried out.

3.2 Basis functions and elements

The way in which the basis functions are created is as follows :

1. The domain is divided in small subregions, the *finite elements*. In \mathbb{R}^3 these elements are triquadratic, isoparametric bricks. (See figure 3.2)
2. The basis functions are piecewise polynomial.
3. The basis functions have small support.

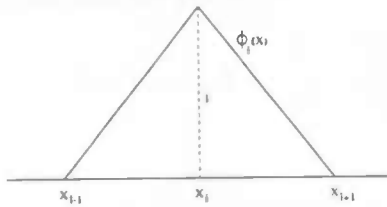


Figure 3.1: linear basis function $\phi_i(x)$, one-dimensional case

4. At specific points, the *nodal points*, the basis functions or their partial derivatives have prescribed values, usually 0 or 1.

In the three-dimensional case, an element consists of 27 nodal points. The intersection of two elements is either an empty set or one common face.

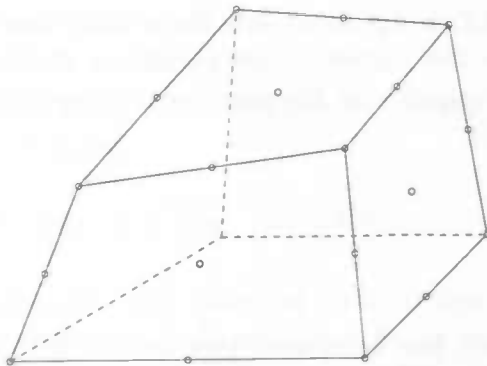


Figure 3.2: three dimensional element with 27 nodal points

In every nodal point the degrees of freedom are taken corresponding with the function to be approximated. Per element a polynomial p_i is constructed such that the unknowns are interpolated in every nodal point. Lagrange interpolation is used in case that only function values are unknown. Hermite interpolation must be applied if also derivatives are unknown. Taking together all those polynomials one gets

$$u_N(x) = \sum_{i=1}^N c_i \phi_i(x)$$

with ϕ_i a basis function.

3.3 The Ritz-method

Consider the boundary problem on Ω with boundary Γ :

$$\begin{aligned} Lu &= f \\ u|_{\Gamma} &= 0 \end{aligned} \tag{3.1}$$

with L a differential operator of order $2m$. On condition that L is linear, self-adjoint and positive definite, the solution of problem (3.1) minimizes the energy functional

$$J[u] = \frac{1}{2} (Lu, u) - (f, u) \tag{3.2}$$

with $u \in V = \{ v \in C^{2m}(\Omega) \mid v|_{\Gamma} = 0 \}$.

By partial integration of $(Lu, v) = (f, v)$, the order of differentiation is lowered, giving

$$a(u, v) = F(v) \quad \forall v \in V$$

with $a(u, v)$ a bilinear form and $F(v) = \int_{\Omega} fv \, d\Omega$. Every bounded, linear functional on a set, which is dense in $H_0^m(\Omega)$, can be extended continuously to the whole Hilbert space $H_0^m(\Omega)$. So, finding the minimum of (3.2) is equal to

$$\min_{u \in H_0^m} J[u], \quad J[u] = \frac{1}{2} a(u, u) - F(u) \tag{3.3}$$

In the Ritz-method there is a N -dimensional subspace $V_N \subset H_0^m(\Omega)$ to choose. V_N is spanned by the linearly independent basis functions ϕ_1, \dots, ϕ_N . The solution of (3.3) must be found on this subspace. Every element $u \in V_N$ can be written as a linear combination of the basis functions.

$$u = \sum_{j=1}^N c_j \phi_j$$

Substituting this in (3.3) yields

$$\begin{aligned} J[u] &= \frac{1}{2} a\left(\sum_{j=1}^N c_j \phi_j, \sum_{j=1}^N c_j \phi_j\right) - \sum_{j=1}^N c_j F(\phi_j) \\ &= \frac{1}{2} \sum_{i,j=1}^N c_i c_j a(\phi_j, \phi_i) - \sum_{j=1}^N c_j F(\phi_j) \end{aligned} \tag{3.4}$$

When $u = \hat{u}_N$ is the solution of the minimization problem, then

$$\frac{\partial J[\hat{u}_N]}{\partial c_i} = 0 \quad i = 1, \dots, N \tag{3.5}$$

This leads to a set of linear equations for the c_i :

$$\sum_{j=1}^N a(\phi_j, \phi_i) c_j = F(\phi_i) \quad i = 1, \dots, N \quad (3.6)$$

or

$$A\mathbf{c} = \mathbf{F} \quad (3.7)$$

with A the stiffness matrix. Solving (3.7) gives the Ritz approximation \hat{u}_N of the solution of problem (3.3).

3.4 The Galerkin method

When the functional L is no longer self adjoint, we can use the weak formulation of problem (3.1)

$$(Lu, v) = (f, v) \quad \forall v \in V \quad (3.8)$$

with V the set of test functions. Using partial integration, there arises again a bilinear form

$$a(u, v) = F(v) \quad \forall v \in V$$

This bilinear form is bounded and positive definite within the Hilbert space H_0^m . Now the Galerkin formulation of (3.8) reads:

$$\text{find } u \in H_0^m \text{ such that } a(u, v) = F(v) \quad \forall v \in H_0^m.$$

There exists a unique solution \hat{u} . The Galerkin method now is used to find an approximation \hat{u}_N of \hat{u} . Therefore there is a N -dimensional, linear subspace $V_N \subset H_0^m$ to choose, spanned by linearly independent basis functions ϕ_1, \dots, ϕ_N . Now look for the linear combination

$$\hat{u}_N = \sum_{j=1}^N c_j \phi_j \quad (3.9)$$

such that

$$a(\hat{u}_N, v) = F(v) \quad \forall v \in V_N$$

Substituting this in equation (3.9) leads to a new system of linear equations for the c_i .

$$\sum_{j=1}^N a(\phi_j, \phi_i) c_j = F(\phi_i) \quad i = 1, \dots, N$$

notated as

$$A\mathbf{c} = \mathbf{F}$$

Solving this gives the approximation \hat{u}_N of \hat{u} .

3.5 The penalty function method

Solving the Navier-Stokes equations takes a lot of computing time and computer memory, due to the presence of the continuity equation (2.1). The idea of the penalty method is to perturb the continuity equation with a small term containing the pressure,

$$\epsilon p + \nabla \cdot \vec{v} = 0 \quad (3.10)$$

with ϵ a small parameter. One can consider this perturbation as the introduction of a slight artificial compressibility. This small parameter ϵ must be chosen such that $\epsilon p = O(10^{-6})$. With this extra term the pressure term can be eliminated, so the pressure becomes a derivative of the velocity. The momentum equation and the continuity equation are now decoupled. After discretizing with the Galerkin method and after eliminating the pressure term from the Navier-Stokes equations, the following system of equations arises:

$$M \frac{\partial u}{\partial t} + S(u)u + N(u)u + \frac{1}{\epsilon} L^T M_p^{-1} L u = F \quad (3.11)$$

with u the discretized velocity vector, M the mass matrix, $S(u)$ the stress matrix and $N(u)u$ the discretization of the convective terms. L represents the divergence matrix. F is a vector which contains parts of the diffusive and pressure terms in the momentum equation due to the boundary. The pressure is computed from:

$$\epsilon M_p p = -L u \quad (3.12)$$

The matrix M_p is termed the pressure mass matrix. Approximation (3.10) can be justified because the continuity equation is satisfied approximately for $\epsilon \rightarrow 0$, due to the finite value of the pressure. A general proof of the fact that the solution of the penalty function method approaches the solution of the unperturbed system can be found in [6].

3.6 Time integration

The term $\frac{\partial u}{\partial t}$ in equation (3.11) must be discretized. This has been done with a finite difference θ -method. The idea of this θ -method is : compute first $u^{n+\theta}$ ($0 \leq \theta \leq 1$) by

$$M \frac{u^{n+\theta} - u^n}{\theta \Delta t} + S(u^n)u^{n+\theta} + N(u^n)u^{n+\theta} + \frac{1}{\epsilon} L^T M_p^{-1} L u^{n+\theta} = F(u^{n+\theta}) \quad (3.13)$$

where $(.)^n$ stands for the n^{th} computed value of $(.)$ in time. Then

$$u^{n+1} = \frac{1}{\theta} u^{n+\theta} - \frac{1-\theta}{\theta} u^n \quad 0 \leq \theta \leq 1 \quad (3.14)$$

and

$$t^{n+\theta} = t^n + \theta \Delta t \quad (3.15)$$

This results in:

$$\begin{aligned} M \frac{\mathbf{u}^{n+1} - \mathbf{u}^n}{\Delta t} + \theta [S + N(\mathbf{u}^{n+1}) + \frac{1}{\epsilon} \mathbf{L}^T \mathbf{M}_p^{-1} \mathbf{L}] \mathbf{u}^{n+1} = \\ F(\mathbf{u}^{n+\theta}) - (1 - \theta) [S + N(\mathbf{u}^n) + \frac{1}{\epsilon} \mathbf{L}^T \mathbf{M}_p^{-1} \mathbf{L}] \mathbf{n}^n \end{aligned} \quad (3.16)$$

The θ -method is conditionally stable for $0 \leq \theta \leq 0.5$. When the penalty function method is used, a timestep of $O(\epsilon)$ must be used in order to get a stable scheme for $\theta < 0.5$. So the values of θ are restricted to the interval $0.5 \leq \theta \leq 1$. For $\theta = 0.5$ the θ -scheme reduces to a modified Crank-Nicolson scheme, which is $O(\Delta t^2)$ accurate for linear systems. For $\theta = 1$ the scheme becomes the Euler Implicit method, which is $O(\Delta t)$ accurate for linear equations.

3.7 The linearizations

In all the sets of differential equations till now a non-linear convection term $N(\mathbf{u})\mathbf{u}$ appears. These non-linear terms must be linearized in order to solve the equations. For SEPRAN there are two techniques available for linearization:

- * Picard linearization (successive substitution)
- * Newton iteration

For the time-dependent problem a linearization per time step is sufficient. For the stationary problem iteration is necessary. This iterative procedure is as follows:

- Start with an approximation \mathbf{u}_0 .
Good starting values are for example:
 - $\mathbf{u}_0 = 0$ in the inner region and \mathbf{u}_0 equal to the boundary conditions on the boundary.
 - \mathbf{u}_0 equal to the solution of the Stokes equations (convective terms neglected).
 - \mathbf{u}_0 equal to the solution of the Navier-Stokes equations for a smaller Reynolds number.
- Compute the solution of the non-linear system of equations.

In the next two subsections these two techniques for the linearization will be discussed.

3.7.1 Picard linearization

The Picard linearization (or successive substitution) linearizes the non-linear convective terms at time level $n+1$ by substituting the solution of the preceding time level in $\mathbf{N}(\mathbf{u}^{n+1})$. The convective terms then become of the form:

$$\mathbf{N}(\mathbf{u}^{n+1})\mathbf{u}^{n+1} = \mathbf{N}(\mathbf{u}^n)\mathbf{u}^{n+1} \quad (3.17)$$

Substituting this in the Navier-Stokes equations, we get

$$\begin{aligned} & (\mathbf{M} + \theta \Delta t [\mathbf{S} + \mathbf{N}(\mathbf{u}^n) + \frac{1}{\epsilon} \mathbf{L}^T \mathbf{M}_p^{-1} \mathbf{L}]) \mathbf{u}^{n+1} = \mathbf{F} \\ & + (\mathbf{M} - (1 - \theta) \Delta t [\mathbf{S} + \mathbf{N}(\mathbf{u}^n) + \frac{1}{\epsilon} \mathbf{L}^T \mathbf{M}_p^{-1} \mathbf{L}]) \mathbf{u}^n \end{aligned} \quad (3.18)$$

$$\mathbf{p}^{n+1} = \frac{1}{\epsilon} \mathbf{M}_p^{-1} \mathbf{L} \mathbf{u}^{n+1} \quad (3.19)$$

One gets the same set of equations when first computing $\mathbf{u}^{n+\theta}$ by:

$$\mathbf{M} \frac{\mathbf{u}^{n+\theta} - \mathbf{u}^n}{\theta \Delta t} = - [\mathbf{S} + \mathbf{N}(\mathbf{u}^n) + \frac{1}{\epsilon} \mathbf{L}^T \mathbf{M}_p^{-1} \mathbf{L}] \mathbf{u}^{n+\theta} + \mathbf{F}(\mathbf{u}^{n+\theta}) \quad (3.20)$$

Then

$$\mathbf{u}^{n+1} = \frac{1}{\theta} \mathbf{u}^{n+\theta} - \frac{1 - \theta}{\theta} \mathbf{u}^n \quad (3.21)$$

with $t^{n+\theta} = t^n + \theta \Delta t$.

3.7.2 Newton iteration

Newton's method is characterized by the fact that it is a quadratically converging process. Therefore, once it converges, it requires only a few iterations. A typical disadvantage of this method is that usually a good estimate is required. Generally, the result of one Picard iteration is a good starting value for the Newton process.

The Newton iteration linearizes the non-linear convective terms in equation (3.16) at time level $n + 1$ as follows

$$\mathbf{N}(\mathbf{u}^{n+1})\mathbf{u}^{n+1} = \mathbf{N}(\mathbf{u}^n)\mathbf{u}^{n+1} + \mathbf{N}(\mathbf{u}^{n+1})\mathbf{u}^n - \mathbf{N}(\mathbf{u}^n)\mathbf{u}^n \quad (3.22)$$

In order to be able to solve the non-linear equations we need to define the Jacobian $\mathbf{J}(\mathbf{u}^n)$ of $\mathbf{N}(\mathbf{u}^n)\mathbf{u}^n$ by

$$\mathbf{J}(\mathbf{u}^n)^{ij}(k, l) = \frac{\partial}{\partial \mathbf{u}_{jl}^n} [\mathbf{N}(\mathbf{u}^n)\mathbf{u}^n]_{ik}$$

The set of non-linear equations can now be solved by:

$$\begin{aligned} (\mathbf{M} + \theta \Delta t [\mathbf{S} + \mathbf{J}(\mathbf{u}^n) + \frac{1}{\epsilon} \mathbf{L}^T \mathbf{M}_p^{-1} \mathbf{L}]) \mathbf{u}^{n+1} &= \mathbf{F}(\mathbf{u}^{n+\theta}) + \\ (\mathbf{M} - (1 - \theta) \Delta t [\mathbf{S} + \frac{1}{\epsilon} \mathbf{L}^T \mathbf{M}_p^{-1} \mathbf{L}]) \mathbf{u}^n - (1 - 2\theta) \Delta t \mathbf{N}(\mathbf{u}^n) \mathbf{u}^n & \end{aligned} \quad (3.23)$$

The pressure can be computed from:

$$\mathbf{p}^{n+1} = \frac{1}{\epsilon} \mathbf{M}_p^{-1} \mathbf{L} \mathbf{u}^{n+1} \quad (3.24)$$

The same set of equations arises when first computing $\mathbf{u}^{n+\theta}$ by:

$$\mathbf{M} \frac{\mathbf{u}^{n+\theta} - \mathbf{u}^n}{\theta \Delta t} = - [\mathbf{S} + \mathbf{J}(\mathbf{u}^n) + \frac{1}{\epsilon} \mathbf{L}^T \mathbf{M}_p^{-1} \mathbf{L}] \mathbf{u}^{n+\theta} + \mathbf{F}(\mathbf{u}^{n+\theta}) \quad (3.25)$$

with $\mathbf{u}^{n+\theta}$ defined as in (3.14).

3.8 Initial and boundary conditions

As mentioned in section 3.7 good starting values for the stationary problem are necessary. During the computations the following procedure was used. Start with $\mathbf{u}_0 = 0$ in the inner region and \mathbf{u}_0 satisfying the boundary conditions on the boundary. In that case the Stokes method was used. After one iteration the linearization was done with Picard, because Newton converges too slow at this point. The absence of the non-linear terms because of Stokes causes this. After the second iteration the solution is so accurate that Newton's method becomes the best choice till the end. In general three or four iterations with Newton's method were necessary. The difference between two successive solutions then became less than 10^{-6} .

The boundary conditions are given by:

- $\vec{v} = 0$ on the wall of the tube (no-slip condition).
- $\vec{v}(x, y)$ is given on the inflow surface ($z = 0$).
- $\sigma \cdot \mathbf{n} = 0$ on the outflow surface (free stress condition).

where σ is the stress tensor. The last condition is a natural boundary condition, in contrast to the other two boundary conditions, which are essential ones. We could have applied an essential boundary condition, but this would mean that we need to know the solution there in advance, which is not the case. This natural boundary condition is satisfied automatically by the applied solution method in a weak sense. The cross-sectional mean velocity in axial direction was chosen in such way that the Reynolds number $Re = 150$ or 300 .

For the time-dependent problem the results of the stationary problem served as initial estimate \mathbf{u}^0 . The velocity on the inflow surface changed into $\vec{v} = \vec{v}(x, y, t)$. Now the time-averaged cross-sectional mean velocity in axial direction was chosen such that $Re = 150$ or 300 .

3.9 Matrix decomposition

After the linearizations and time integrations we have a large set of equations. The solution on a new time level are computed numerically using the θ -method:

1. $M \frac{u^{n+\theta} - u^n}{\theta \Delta t} + [S'(u^n) + N'(u^n) + \frac{1}{\epsilon} L^T M_p^{-1} L] u^{n+\theta} = F(u^{n+\theta})$
2. $u^{n+1} = \frac{1}{\theta} u^{n+\theta} - \frac{1-\theta}{\theta} u^n$

with $S'(u^n)$ and $N'(u^n)$ the results of the Picard or Newton linearization. Now define A and b as:

$$A = M + \theta \Delta t [S'(u^n) + N'(u^n) + \frac{1}{\epsilon} L^T M_p^{-1} L]$$

$$b = M + \theta \Delta t F(u^{n+\theta})$$

The set of equations reduces to $Ax = b$, in which $x = u^{n+\theta}$ is the only remaining unknown. The matrix A has a band structure depending on the basis functions $\phi(x)$. Using the Gaussian Elimination algorithm the linear set $Ax = b$ can be solved. A new system $Ux = g$ is formed, with U an upper triangular matrix. This new system can be solved using the back-substituting process. The unknown g is the solution of $Lg = b$. L is a lower triangular matrix, which has ones on its diagonal. Pivoting is not necessary due to the fact that the penalty function method is used. A complete description of the Gaussian Elimination algorithm or the LU -decomposition can be found in [1].

Chapter 4

Results

In this chapter the results of the computations are given. In the first section a stationary flow is discussed. It will be indicated how long one solid tube can be made on the computer system, when one looks at the required computer memory space. Furthermore an estimation of the error between the outcomes of the computations in one tube and several tubes will be given. In the second section the same will be done for an unsteady flow. In section 4.3 flows with secondary velocity are introduced. Again stationary and instationary flows are considered. Some of the velocity plots are presented in chapter 5. The length of the tubes is always expressed in diameters. When several tubes are placed behind each other, the total axial distance is expressed in diameters.

4.1 Stationary flow

The computations of a stationary flow need relatively little computer memory space. The maximum length of one tube is about 7 times the diameter. However, this length is too short, because the flow isn't fully developed after 7 times the diameter. Therefore we introduced the principle to put several tubes after each other. The advantage of this principle is that the required computer memory space was far less and that there is a great gain of time, as can be seen in table 4.1. The question is whether this principle is a good one, concerning the accuracy. Therefore an estimation of the error is made. This has been

Table 4.1: comparison between the computation in one tube and several tubes

# tubes	length	memory space	time
1	6	388 MB	7h. 26 min.
3	2	130 MB	3h. 25 min.
4	1.5	94 MB	3h. 10 min.
6	1	35 MB	56 min.

Table 4.2: Norm of the differences between the velocity in one tube and several tubes, in percents. $Re = 300$

# diam.	3×2 diam.		4×1.5 diam.		6×1 diam.	
	a	b	a	b	a	b
1					.43	.25
2	.34	.18			.70	.42
3			.56	.39	1.05	.67
4	.31	.33			1.46	.95
5					1.83	1.24
6	.82	.79	.93	.84	2.26	1.59

done by comparing the results of the computations in one tube with the results of the computations in several tubes and by comparing the results of the computations in several tubes with the Poiseuille profile, into which the flow must develop. The results of the comparison between the results in one tube and several tubes can be found in table 4.2. The norm used is the L_2 norm. The difference between both methods has been computed by taking the norm of the relative difference in the axial velocity in the grid points on an intersection of the tube at $z = n$ times the diameter: $\|(v_1 - v_2)/v_1\|_2$. So the differences between both methods are given in percents with respect to what the result should be. To get the computational results, two different inflow profiles are used, which are shown in figure 4.1 & 4.2. The “double-hump” profile in figure 4.1 is representative for the inflow profile in the basilar artery, which results from the merging of the two flows from the two vertebral arteries (see the figure on page 5). The profile in figure 4.2 is a parabolic (Poiseuille) profile. In figure 5.1 on page 33 the velocity profiles for inflow profile (a) are presented after being computed in one tube of length 6 times the diameter.

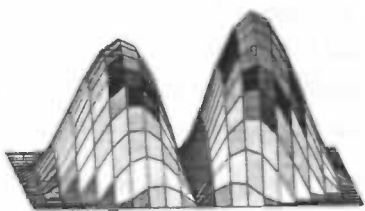


Figure 4.1: inflow profile (a)

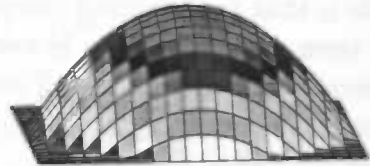


Figure 4.2: inflow profile (b)

Each flow in a tube will eventually become a Poiseuille flow, no matter what its inflow profile is. This is another way to check the correctness of the principle to place tubes behind each other. Therefore, several tubes are placed behind each other such that the total length of the tube was 30 times the diameter. For inflow profile (a) the results are given in figure 4.3. The development of the velocity is plotted in figure 5.2.

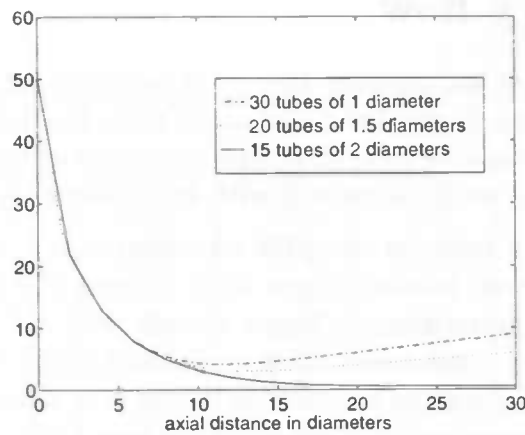


Figure 4.3: Norm of the differences between the computed flow and the Poiseuille flow, in percents. $Re = 300$

As can be seen in figure 4.3 the velocity perfectly develops into a Poiseuille flow, when 15 tubes of 2 diameters are used. In all other cases the difference is larger. When the inflow profile is Poiseuille, it should stay Poiseuille. In figure 4.4 the differences between the Poiseuille inflow profile and the computed results are given. Per transition the norm of the difference grows about 0.3%.

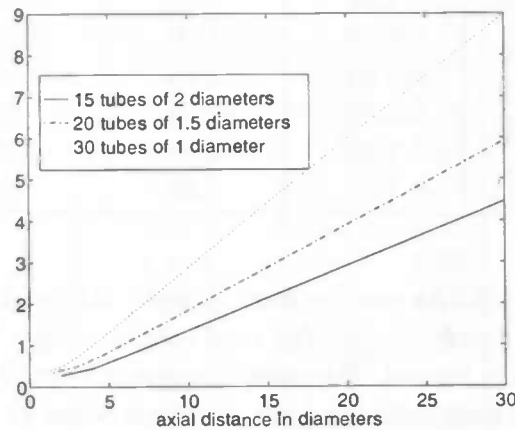


Figure 4.4: Norm of the differences between the computed flow and the Poiseuille inflow profile, in percents. $Re = 300$

4.2 Instationary flow

In this section the results of instationary flows will be discussed. We'll have a look at the results of the computations in one tube compared with the results of the computations in several tubes. Furthermore we look at the development of the flow downstream, when several tubes are used, and we'll compare it with the Womersley profile (see section 2.3).

The maximum length of a tube to compute an instationary, three-dimensional flow, is about 4 diameters. However, a tube longer than 3 times the diameter was never used, because the required computer memory space already was 256 MB. An estimate for the required computer memory space when using a tube of 4 diameters is about 420 MB. The computer *CIWI10* might be able to handle this, but it was never tried, because we didn't want to load the computer system that heavily for a long time. To compare the results of the computations, two different inflow profiles were used. The first profile was an oscillating Poiseuille flow and the second profile was an oscillating flow that was uniformly distributed on the inflow surface. The axial velocity is assumed to oscillate like $1 + \frac{1}{2} \sin(2\pi t)$, which means that the frequency of the oscillation is 1 Hz. and the relative amplitude is $\frac{1}{2}$.

The difference between the velocity computed in one tube of three diameters and the velocity computed in three successive tubes of one diameter is given in the tables 4.3 & 4.4. In both cases $\delta t = \frac{1}{12}$. The evolution of the flow is presented in figure 5.3 till 5.20 on page 34 to 38. When the time step is decreased to $\delta t = \frac{1}{24}$, the corresponding differences

Table 4.3: norm of the differences in percents. Inflow is Poiseuille. $\delta t = \frac{1}{12}$. $Re = 300$

time	diameter 1	diameter 2	diameter 3
$\frac{1}{12}$	1.30	1.56	3.01
$\frac{1}{4}$	9.46	4.09	3.84
$\frac{5}{12}$	13.64	7.86	8.61
$\frac{7}{12}$	10.86	10.14	11.22
$\frac{3}{4}$	2.20	3.88	4.49
$\frac{11}{12}$	7.67	7.06	7.34

are given in table 4.5 & 4.6. As can be seen in both tables the differences between both methods is greater than for $\delta t = \frac{1}{12}$. An explanation might be that there are twice as much transitions when δt is halved. For each transition a small error has been made. This explains the greater difference between both methods when $\delta t = \frac{1}{24}$, although the method is $O(\delta t)$. To compare the results with a stationary flow, the norm of the differences between the results computed in one tube with length three diameters and three successive tubes of one diameter is given in table 4.7. In table 4.8 the norm of the difference between the results in one tube and those in two tubes of 1.5 diameters is given. As can be seen in all the tables, the difference between the results in one tube and those in several tubes is the greatest when the flow accelerates from the lowest velocity to the maximum.

Table 4.4: norm of the differences in percents. Inflow is flat. $\delta t = \frac{1}{12}$. $Re = 300$

time	diam. 1	diam. 2	diam. 3
$\frac{1}{12}$	2.73	3.41	3.93
$\frac{1}{6}$	1.79	2.02	2.25
$\frac{1}{4}$	1.53	1.57	1.73
$\frac{1}{3}$	1.58	1.67	2.01
$\frac{5}{12}$	1.70	1.87	2.43
$\frac{1}{2}$	1.90	1.94	2.63
$\frac{7}{12}$	2.75	2.15	2.28
$\frac{2}{3}$	5.23	4.29	2.99
$\frac{3}{4}$	8.36	8.21	7.12
$\frac{3}{5}$	8.95	9.98	9.89
$\frac{11}{12}$	6.72	8.29	8.69
1	4.05	5.44	6.28

Table 4.5: norm of the differences in percents. Inflow is flat. $\delta t = \frac{1}{24}$. $Re = 300$

time	diam. 1	diam. 2	diam. 3
$\frac{1}{12}$	4.25	4.45	4.87
$\frac{1}{6}$	4.61	4.68	4.99
$\frac{1}{4}$	4.94	5.14	5.63
$\frac{1}{3}$	5.12	5.46	6.15
$\frac{5}{12}$	5.09	5.53	6.38
$\frac{1}{2}$	4.71	5.15	6.05
$\frac{7}{12}$	4.05	4.29	4.89
$\frac{2}{3}$	4.95	5.47	5.29
$\frac{3}{4}$	8.01	9.78	10.06
$\frac{5}{6}$	8.55	11.14	12.27
$\frac{11}{12}$	6.26	8.52	9.92
1	4.46	5.57	6.58

Table 4.6: norm of the differences in percents. Inflow is Poiseuille. $\delta t = \frac{1}{24}$. $Re = 300$

time	diam. 1	diam. 2	diam. 3
$\frac{1}{12}$	1.13	1.32	3.58
$\frac{1}{6}$	3.84	3.47	2.29
$\frac{1}{4}$	5.46	6.36	6.01
$\frac{1}{3}$	6.45	8.14	8.46
$\frac{5}{12}$	6.89	8.99	9.74
$\frac{1}{2}$	6.29	8.42	9.49
$\frac{2}{7}$	3.40	5.32	6.73
$\frac{2}{12}$	4.28	3.76	3.11
$\frac{3}{12}$	12.92	12.71	10.91
$\frac{4}{12}$	15.53	17.12	16.12
$\frac{6}{12}$	10.45	14.03	14.39
1	3.62	7.52	9.35

Table 4.7: norm of the differences in percents. Inflow is stationary. $Re = 300$

inflow	diam. 1	diam. 2	diam. 3
Poiseuille	.25	.42	.67
Flat	.97	.75	1.06

Table 4.8: Norm of the differences after 3 diameters in percents. Inflow is flat. $\delta t = \frac{1}{12}$. $Re = 300$

time	2 tubes of 1.5 diameters
$\frac{1}{12}$	5.00
$\frac{1}{6}$	4.45
$\frac{1}{4}$	4.51
$\frac{3}{5}$	4.81
$\frac{12}{12}$	5.15
$\frac{1}{2}$	5.36
$\frac{2}{7}$	5.05
$\frac{2}{12}$	4.26
$\frac{3}{12}$	6.15
$\frac{4}{12}$	8.77
$\frac{5}{12}$	8.42
1	6.48

4.2.1 Womersley profile

As explained in section 2.3 far downstream the flow develops to the Womersley profile. In figure 5.21 & 5.22 the computed flow after 10 diameters and the Womersley profile are given. The computations have been made in 10 tubes of 1 diameter and for both inflow profiles. The norm of the differences between the computed flow and the Womersley profile is given in table 4.9.

Table 4.9: norm of the differences between the Womersley profile and the computed flow after 10 diameters, in percents. $Re = 300$

time	norm when inflow profile is Poiseuille	norm when inflow profile is flat
0	12.66	12.75
$\frac{1}{12}$	7.47	7.29
$\frac{1}{6}$	3.76	4.15
$\frac{1}{4}$	4.96	5.93
$\frac{1}{3}$	8.03	8.76
$\frac{5}{12}$	10.05	10.21
$\frac{1}{2}$	9.58	8.90
$\frac{2}{3}$	5.14	3.89
$\frac{1}{12}$	5.52	7.76
$\frac{4}{3}$	15.11	17.19
$\frac{5}{6}$	19.31	20.68
$\frac{11}{12}$	17.44	6.32

There are relatively large differences between the computed values and the Womersley profile. An explanation might be that the tube of 10 diameters is too short for the flow to be fully developed (see section 2.3). In [5] the inlet length for a pulsating entry flow has been calculated. The inlet length is defined as the distance from the entrance to the point where the centerline velocity deviates 1% from the fully developed value. The inlet length is about 15 to 20 times the diameter. After 10 diameters, the difference is up to 15 %. Another explanation is the fact that a numerical error is made. As can be seen in figure 4.3 & 4.4 an error appears after each transition. This error influences the results negatively. This might explain the unequal surfaces under the velocity plots in figure 5.21 & 5.22.

4.3 Computations with a secondary velocity field

In this section the results of the computations with secondary velocity are given. In the first subsection the flow is stationary and in subsection 4.3.2 an instationary flow is considered. All velocities oscillate like $1 + \frac{1}{2} \sin 2\pi t$. In subsection 4.3.3 the prescribed inflow velocity field oscillates like the heartbeat that is observed in the basilar artery. The prescribed secondary velocity at the entrance of the basilar artery is plotted in figure 4.5.

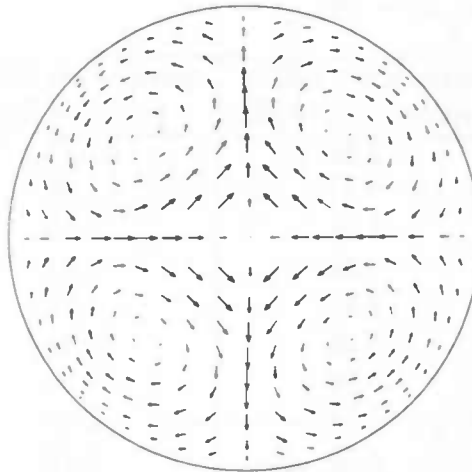


Figure 4.5: secondary velocity

The secondary velocity is given by (if $x \neq 0$ and $y \neq 0$):

$$\begin{aligned}
 \alpha &= \arctan(|x|/|y|) \\
 r &= \sqrt{x^2 + y^2} \\
 v_{tan} &= \text{signum}(x) \sin((r - 0.6)\pi) \\
 v_{rad} &= -\sin(\alpha - \frac{\pi}{4}) (1 - r^{10}) \\
 u &= (\cos(\alpha) v_{tan} + \text{signum}(x) \sin(\alpha) v_{rad}) (1 - r^6) \\
 v &= (-\text{signum}(x) \text{signum}(y) \sin(\alpha) v_{tan} + \text{signum}(y) \cos(\alpha) v_{rad}) (1 - r^6)
 \end{aligned}$$

Along both axes the velocity is given by:

$$\begin{aligned}
 u &= -\cos((x - 0.5)\pi) \quad (\text{if } y = 0) \\
 v &= \cos((y - 0.5)\pi) \quad (\text{if } x = 0)
 \end{aligned}$$

The secondary velocity field as in figure 4.5 is caused by the bends in the vertebral arteries. The fluid in those arteries flows to the outside of the bend, from where it flows along the wall to the innerside of the bend. When the flow is instationary, the secondary velocity field has the same frequency and relative amplitude as the oscillation in axial direction.

4.3.1 Stationary flow

For a stationary flow the magnitude of the maximum secondary velocity compared with the magnitude of the mean axial velocity is taken about 25% and 50%. The results can be found in figure 5.23 & 5.24. The plots are made at the inflow surface and after 1,2,4,6,8,10 and 12 times the diameter. The secondary velocity at the same places are given in figure 5.25 & 5.26. In figure 5.27 till 5.30 velocity profiles in the cross-sections along both axes are given. All results agree with the flow phenomena described in [9].

4.3.2 Instationary flow

In this section the results of an instationary flow with secondary velocity are given. The magnitude of the secondary velocity is about 50% of the mean velocity in axial direction, which corresponds with the magnitude of the secondary velocity in the basilar artery. The frequency and the relative amplitude of the oscillation of the secondary velocity are the same as those of the oscillation of the axial velocity. In figure 5.31 till 5.36 the axial velocity is plotted for some points in time. The plots are made at the inflow surface and after 1,2 and 3 times the diameter. In figure 5.37 & 5.38 velocity profiles in the cross-sections along the x and y axes are given. The cross-sections are also made at the inflow surface and after 1,2 and 3 times the diameter. The plots are given for one period and the timestep is $\frac{1}{12}$. In figure 5.39 till 5.41 the secondary velocity is plotted.

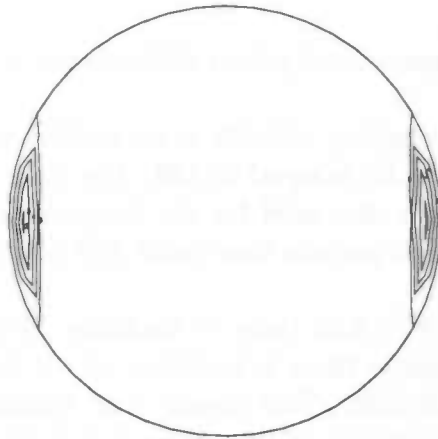


Figure 4.6: recirculation regions when the entry flow is oscillating. $t = \frac{2}{3}$ and $z = 3$ times the diameter. $Re = 300$

For $t = \frac{2}{3}$ and for $z = 3$ times the diameter there is backflow. In figure 4.6 a contour plot of the negative velocity is given. The recirculation are situated at the ends of the x -axis. The magnitude of the negative velocity is up to 4.7% of the mean axial velocity at this particular time.

4.3.3 The pulses of the heart

The inflow of all instationary flows considered till now oscillated like $1 + \frac{1}{2}\sin(2\pi t)$. Now we look at a heart beat that is observed in the basilar artery. The cross-sectional mean velocity is given in figure 4.7 for 4 periods. Also the secondary velocity oscillates like in

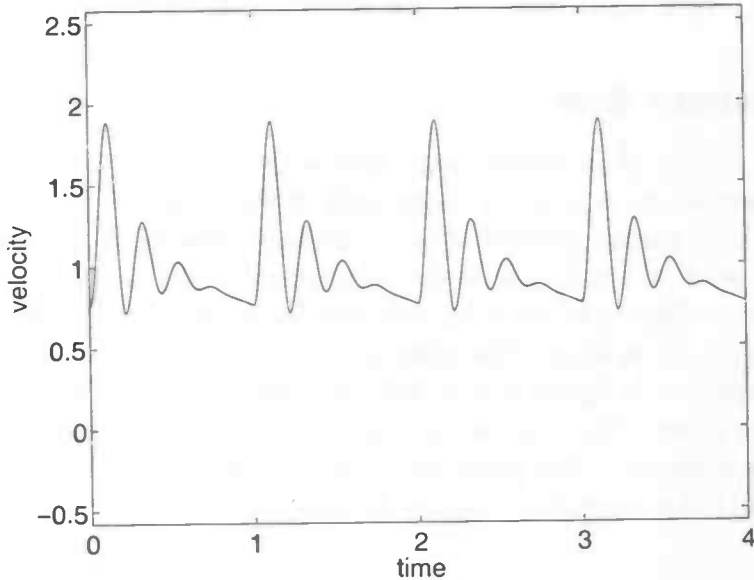


Figure 4.7: The normalized pulses of the heart in the basilar artery

figure 4.7. The maximum secondary velocity is up to 50% of the mean axial velocity, for every t . The Reynolds number Re is equal to 150. The results of the computations can be found from page 51. The time step used for the computations was $\delta t = 0.01$. The total computation time to simulate 4 periods was about 138 hours.

As can be seen in figure 5.55 & 5.56 there is backflow. This occurs at all intersections. After 1 and 2 times the diameter there is backflow at $t = 0.18$ till 0.24 and after 3 times the diameter at $t = 0.18$ till 0.22. This means that backflow occurs when the velocity is about to reach its lowest velocity, after a period of decelerating. Contour plots of the negative axial velocity can be found in the figures on page 55 & 56. At $t = 0.2$ and after 1 diameter the most negative axial velocity is about 25 % of the mean axial velocity at that time. Backflow after 3 times the diameter can be physically correct, but for the model used it might be incorrect. The tube in which the flow is simulated, is no longer than 3 times the diameter. When there is backflow at the outflow plane, there is a flow from "outside". It seems to be no problem, but maybe the results are not completely correct.

After this a pulsating flow without prescribed secondary velocity has been computed. Again backflow occurs. The contour plots of the negative velocity can be found in figure 5.65 till 5.67. The intersections of the axial velocity along both axes can be found in the figures on the pages 62 & 63. The differences between the results of the computations with and without a prescribed secondary velocity field are clear. With the secondary velocity as defined before the fluid with the highest axial velocity is driven into the middle of the tube. The cross-sections along the x -axis in figure 5.55 show that the velocity in the middle of the tube is higher than the velocity in the middle of the tube when there is no prescribed secondary velocity. The influences of the secondary velocity field are also very clear when comparing the contour plots of the negative velocity. A pulsating flow with prescribed secondary velocity field mainly has backflow in the regions at the ends of the x -axis, whereas a pulsating flow without prescribed secondary velocity has recirculation regions almost everywhere near the wall of the tube. The backflow in this case is stronger at the regions at the ends of the y -axis, because of the inflow profile that is used.

A pulsating flow with secondary velocity and with Reynolds number $Re = 300$ has also been computed. In figure 5.70 & 5.71 the cross-sections of the velocity profiles along the x and y axes are given. As can be seen backflow occurs. The recirculation regions are presented on page 66 & 67. The position of the recirculation regions in this case is more concentrated near the ends of the x -axes than for $Re = 150$. There is also a move of these regions in axial direction, because of the larger inflow velocity. The magnitude of the negative axial velocity is about twice as great as the magnitude of the negative axial velocity when $Re = 150$.

Chapter 5

Figures

In this chapter some of the plots are presented. The plots refer to the results in chapter 4. On the left hand the development of the flow in a tube of length 6 times the diameter is presented. The velocity profiles are given after each diameter. The inflow profile is the “double-hump” profile as mentioned in section 4.1. On the right hand the results are computed in tubes of length 2 times the diameter. The profiles are given at the inflow surface and after 2, 4, 6, 8, 10 and 12 times the diameter.

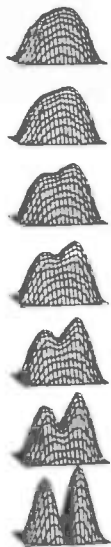


Figure 5.1: development of the flow with “double-hump” inflow profile. The Reynolds number $Re = 300$.



Figure 5.2: development of the flow computed in tubes of length 2 times the diameter. The results are presented at $z = 0, 2, 4, 6, 8, 10$ and 12 times the diameter.

The velocity plots for an oscillating Poiseuille inflow profile, as discussed in section 4.2, are given below. The frequency of the oscillation is 1 Hz. and the relative amplitude is 0.5. The time is successively $t = \frac{1}{12}, \frac{1}{4}, \frac{5}{12}, \frac{7}{12}, \frac{3}{4}$ and $\frac{11}{12}$. The plots are given after 1, 2 and 3 diameters. On the left hand the plots are made from the results of the computations in one tube, whereas on the right hand they are made of the results in three tubes of 1 diameter. The Reynolds number $Re = 300$.

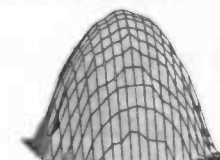
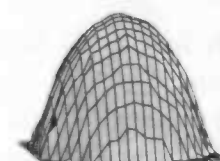
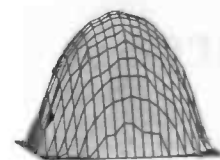
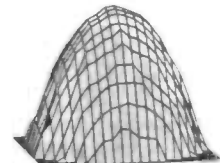
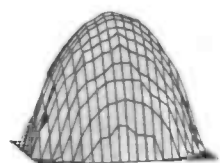
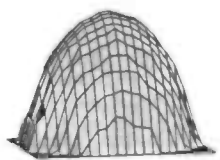


Figure 5.3: $t = \frac{1}{12}$

Figure 5.4: $t = \frac{1}{12}$

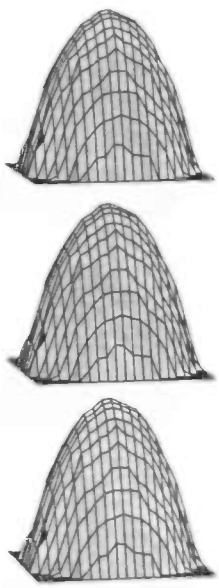


Figure 5.5: $t = \frac{1}{4}$

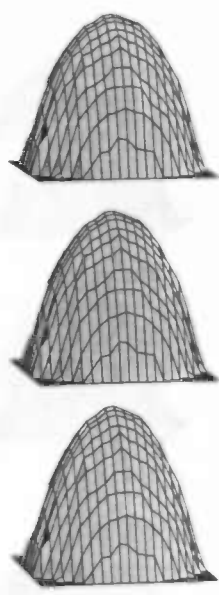
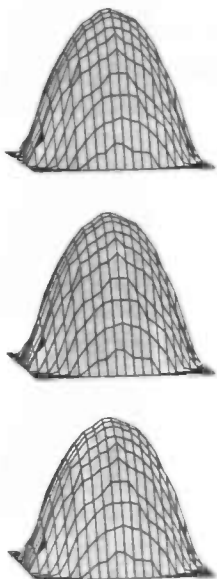
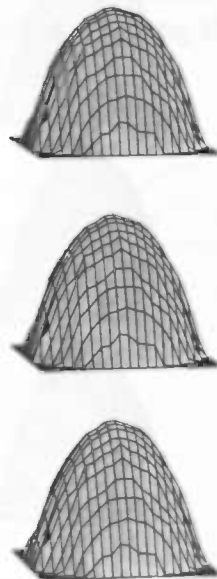


Figure 5.6: $t = \frac{1}{4}$

Figure 5.7: $t = \frac{5}{12}$ Figure 5.8: $t = \frac{5}{12}$ Figure 5.9: $t = \frac{7}{12}$ Figure 5.10: $t = \frac{7}{12}$

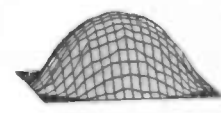
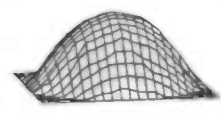
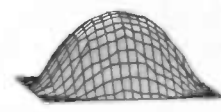
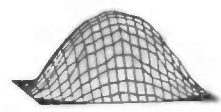
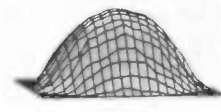
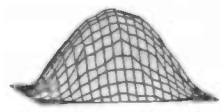


Figure 5.11: $t = \frac{3}{4}$

Figure 5.12: $t = \frac{3}{4}$

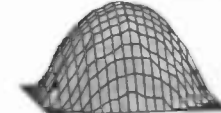
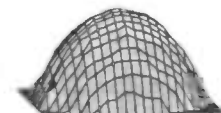
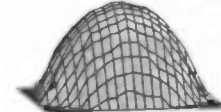
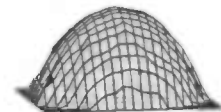
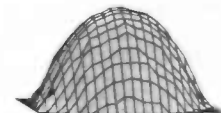
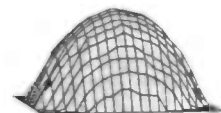


Figure 5.13: $t = \frac{11}{12}$

Figure 5.14: $t = \frac{11}{12}$

Velocity plots for an oscillating inflow profile, which is uniform on the inflow surface. The frequency of the oscillation is 1 Hz. and the relative amplitude is 0.5. The results are given for $z = 0$ till 10 times the diameter. The plots are made of cross-sections along the x axis. The flow is axially symmetric. The Reynolds number $Re = 300$.

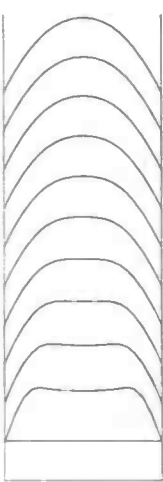


Figure 5.15: $t = 0$

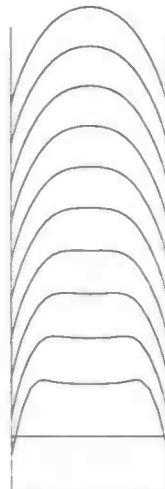


Figure 5.16: $t = \frac{1}{6}$

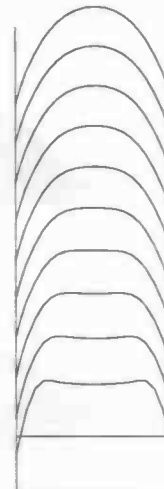


Figure 5.17: $t = \frac{1}{3}$

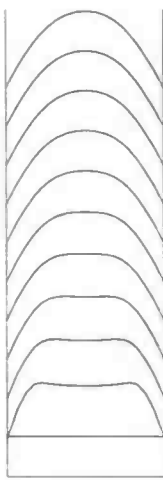


Figure 5.18: $t = \frac{1}{2}$

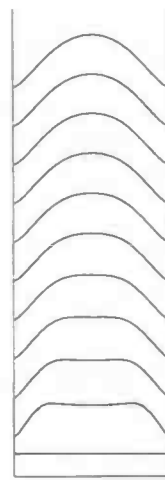


Figure 5.19: $t = \frac{2}{3}$

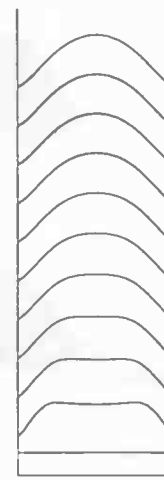


Figure 5.20: $t = \frac{5}{6}$

In the next velocity plots the computed flow after 10 diameters and the Womersley profile according to the theory are given. The computations have been made in 10 tubes of one diameter (see section 4.2.1). In figure 5.21 the inflow profile is an oscillating Poiseuille flow, whereas in figure 5.22 the inflow profile is flat. In both cases the Reynolds number $Re = 300$.

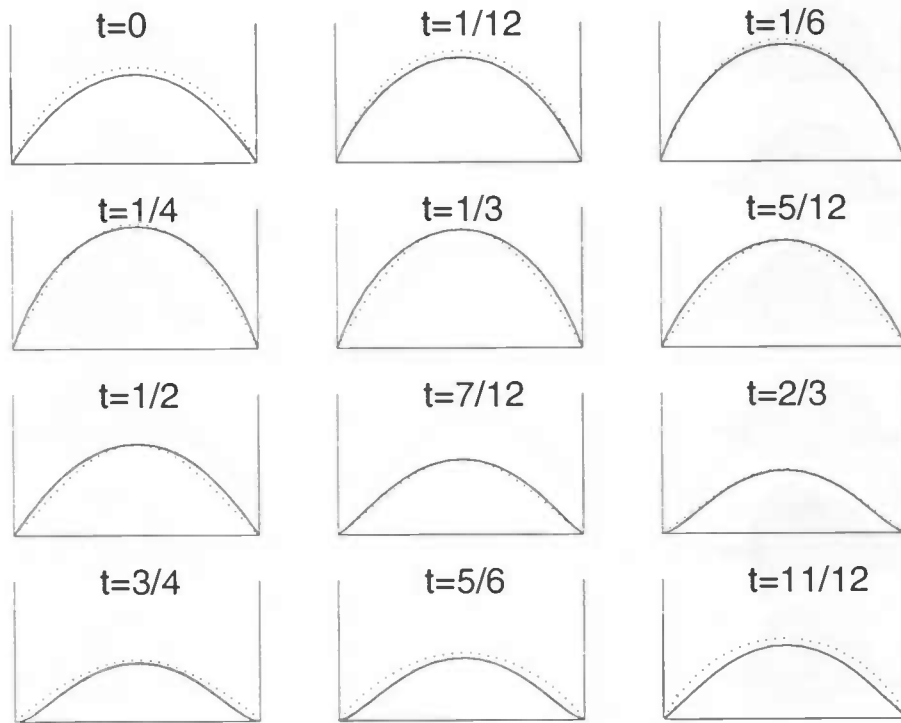


Figure 5.21: Velocity plots for several time steps. \cdots : Womersley profile, $-$: computed flow

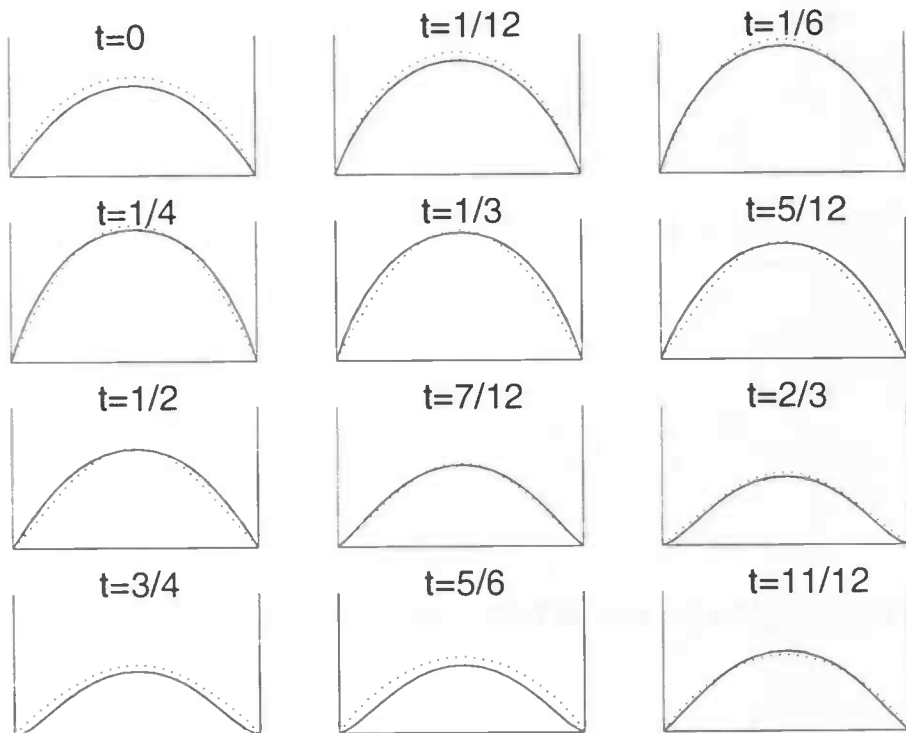


Figure 5.22: Velocity plots for several time steps. ···: Womersley profile, —: computed flow

In the next plots the axial velocity is given when there is a secondary velocity. The flow is stationary. The plots are given at the inflow surface and after 1,2,4,6,8,10 and 12 times the diameter. At the left hand the maximum magnitude of the secondary velocity is about 25 % of the mean axial velocity, whereas on the right hand it is about 50 %.

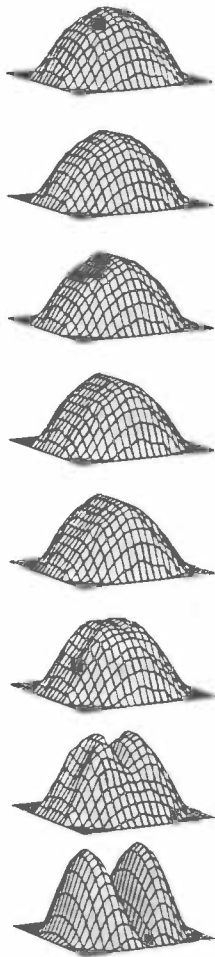


Figure 5.23: Velocity plot when the secondary velocity is about 25 % of the mean axial velocity. $Re = 300$

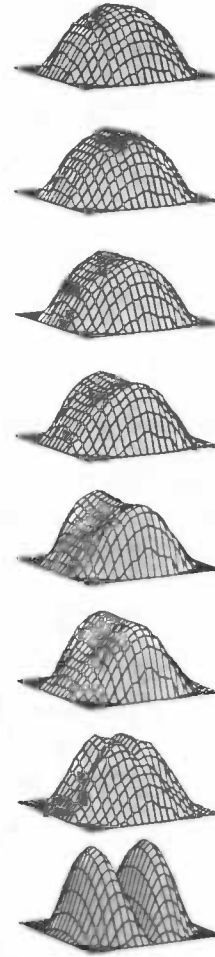


Figure 5.24: Velocity plot when the secondary velocity is about 50 % of the mean axial velocity. $Re = 300$

In the next plots the secondary velocity of a stationary flow is given. The arrow above indicates the magnitude of the mean axial velocity. The Reynolds number $Re = 300$.

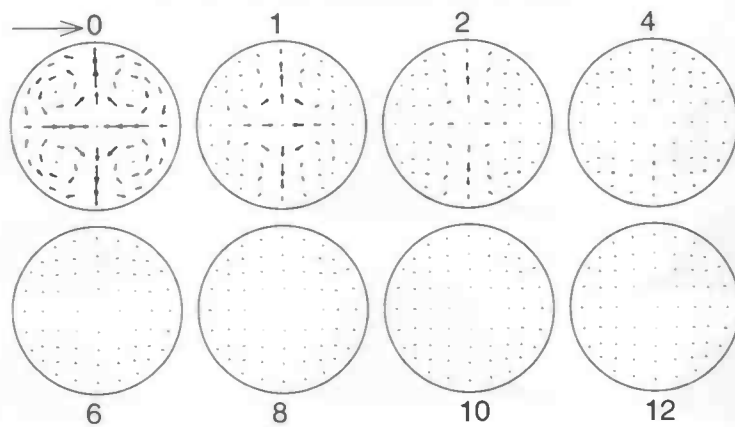


Figure 5.25: secondary velocity when the secondary velocity is about 25 % of the mean axial velocity

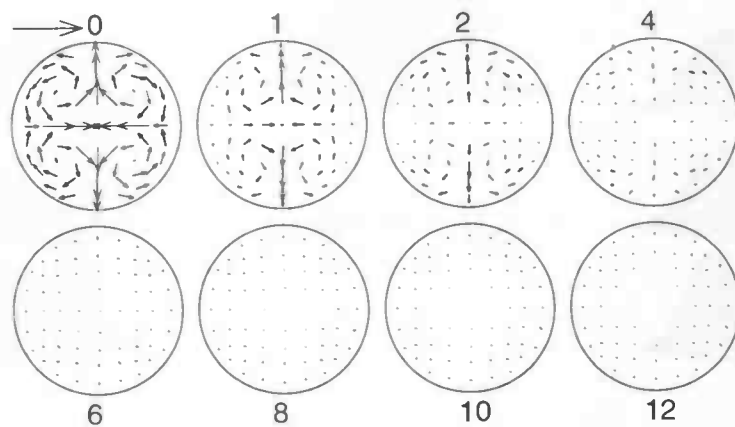


Figure 5.26: secondary velocity when the secondary velocity is about 50 % of the mean axial velocity

In the next plots the cross-sections of the velocity profiles along the x and y axes are given. The cross-sections have been made after diameter 0 till 12. In the upper two plots the maximum secondary velocity is about 25 % of the mean axial velocity and in the other two plots the maximum secondary velocity is about 50% of the mean axial velocity. The flow is stationary.



Figure 5.27: cross-section of the velocity along the x axis when the secondary velocity is about 25 %. $Re = 300$



Figure 5.28: cross-section of the velocity along the y axis when the secondary velocity is about 25 %. $Re = 300$



Figure 5.29: cross-section of the velocity along the x axis when the secondary velocity is about 50 %. $Re = 300$



Figure 5.30: cross-section of the velocity along the y axis when the secondary velocity is about 50 %. $Re = 300$

In the next plots the axial velocity of an instationary flow with secondary velocity is given. The flow oscillates like $1 + \frac{1}{2} \sin(2\pi t)$ (see section 4.3.2). The plots are made at the inflow surface and after 1,2 and 3 times the diameter. The timestep is $\frac{1}{12}$ and the plots are given for $t = 0, \frac{1}{6}, \frac{1}{3}, \frac{1}{2}, \frac{2}{3}$ and $\frac{5}{6}$. The Reynolds number $Re = 300$.

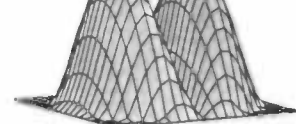
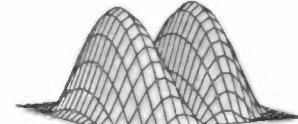
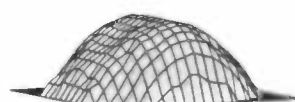
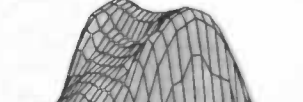
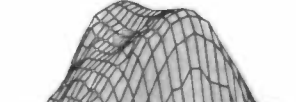
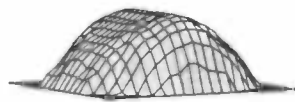
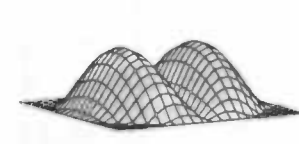
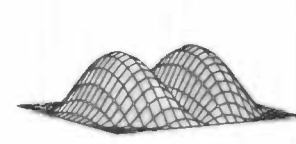
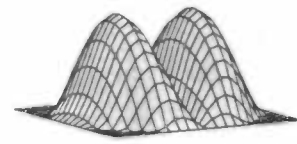
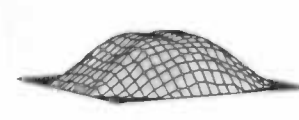
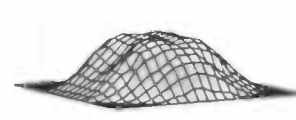
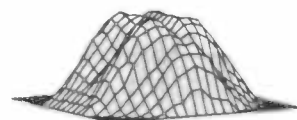
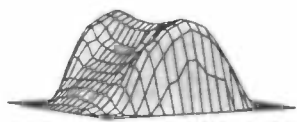


Figure 5.31: $t = 0$

Figure 5.32: $t = \frac{1}{6}$

Figure 5.33: $t = \frac{1}{3}$

Figure 5.34: $t = \frac{1}{2}$ Figure 5.35: $t = \frac{2}{3}$ Figure 5.36: $t = \frac{5}{6}$

In the next plots the cross-sections of the axial velocity of an instationary flow along the x and y axes are given (The picture on the left are the cross-sections of a stationary flow). The cross-sections are made at the inflow surface and after 1,2 and 3 times the diameter. The plots are made for one period with $\delta t = \frac{1}{12}$.

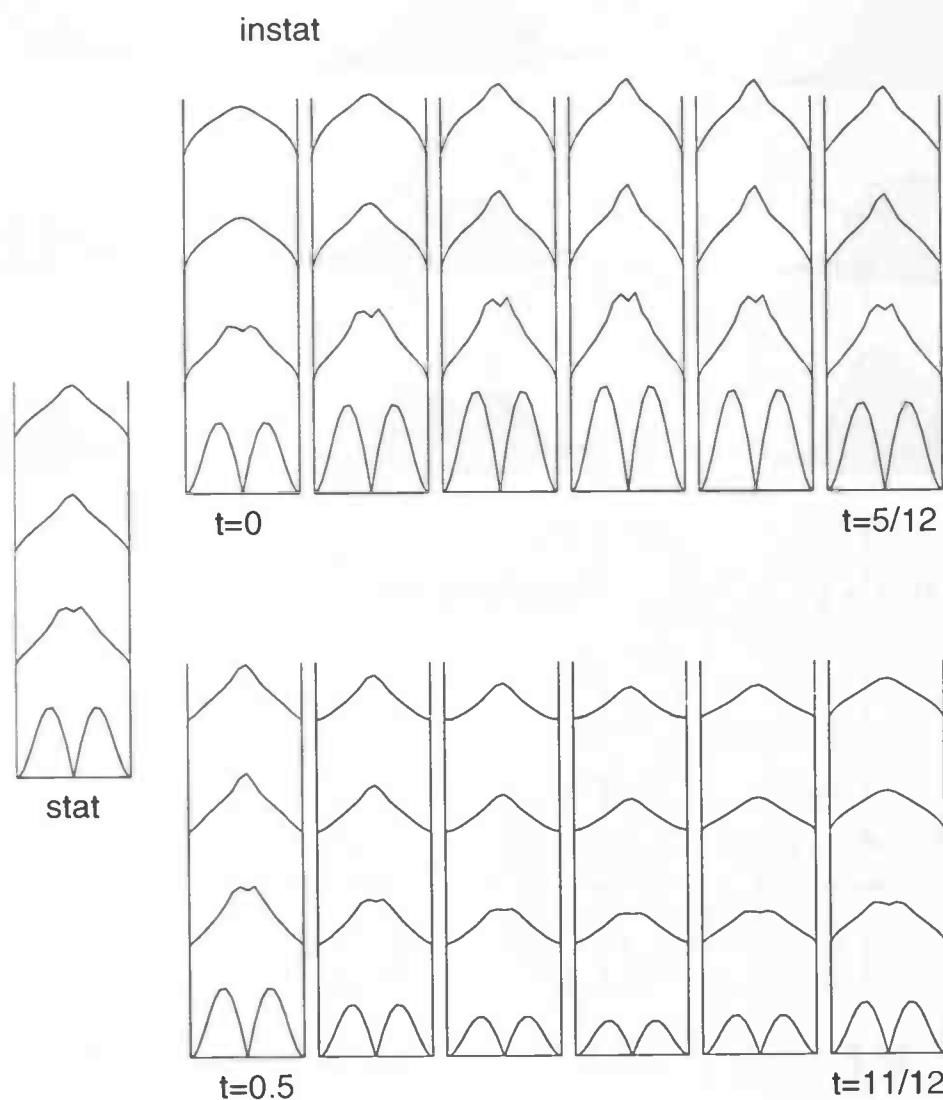


Figure 5.37: The cross-section along the x axis of an instationary flow. $\delta t = \frac{1}{12}$. $Re = 300$

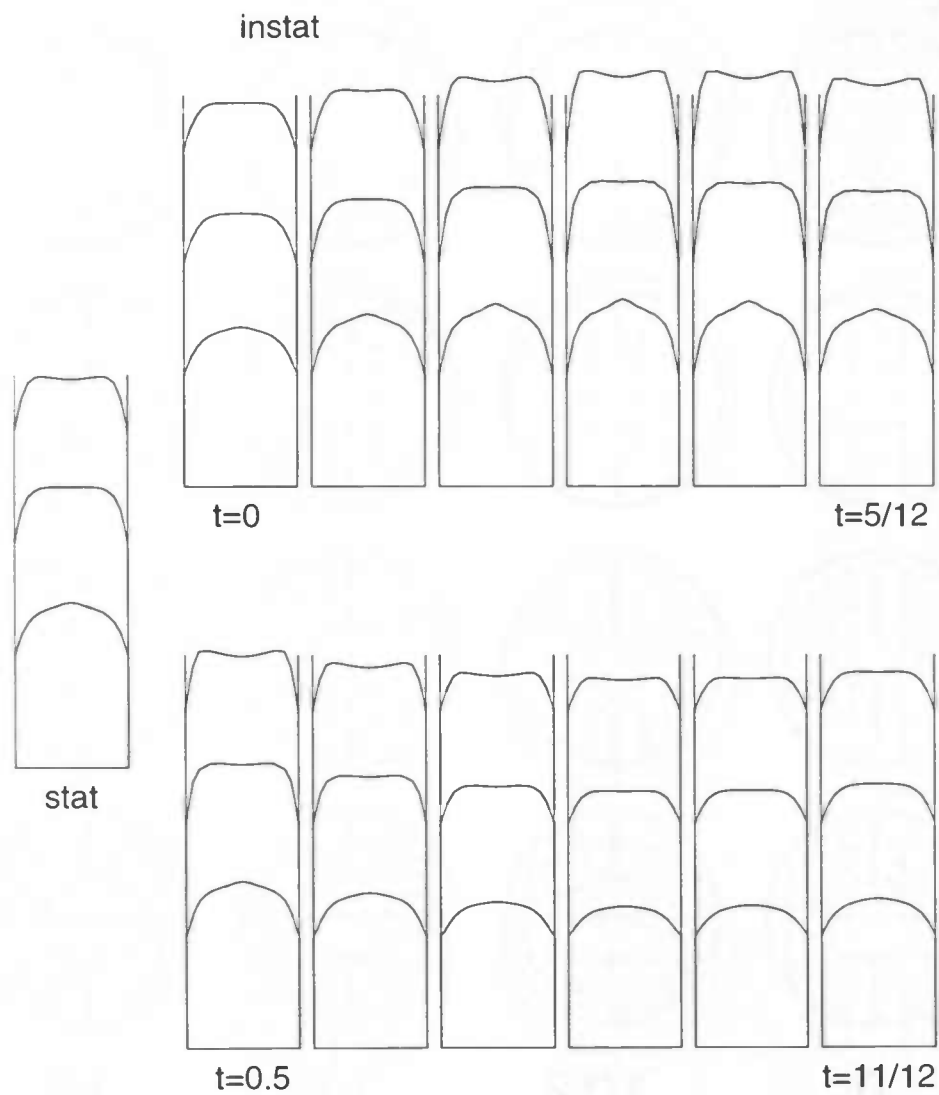


Figure 5.38: The cross-section along the y axis of an instationary flow. $\delta t = \frac{1}{12}$. At the inflow surface the velocity along the y axis is equal to 0. $Re = 300$

In the next plots the secondary velocity is given. The plots are made at the inflow surface and after 1,2 and 3 times the diameter. The arrow above indicates the magnitude of the time averaged mean axial velocity. The Reynolds number $Re = 300$.

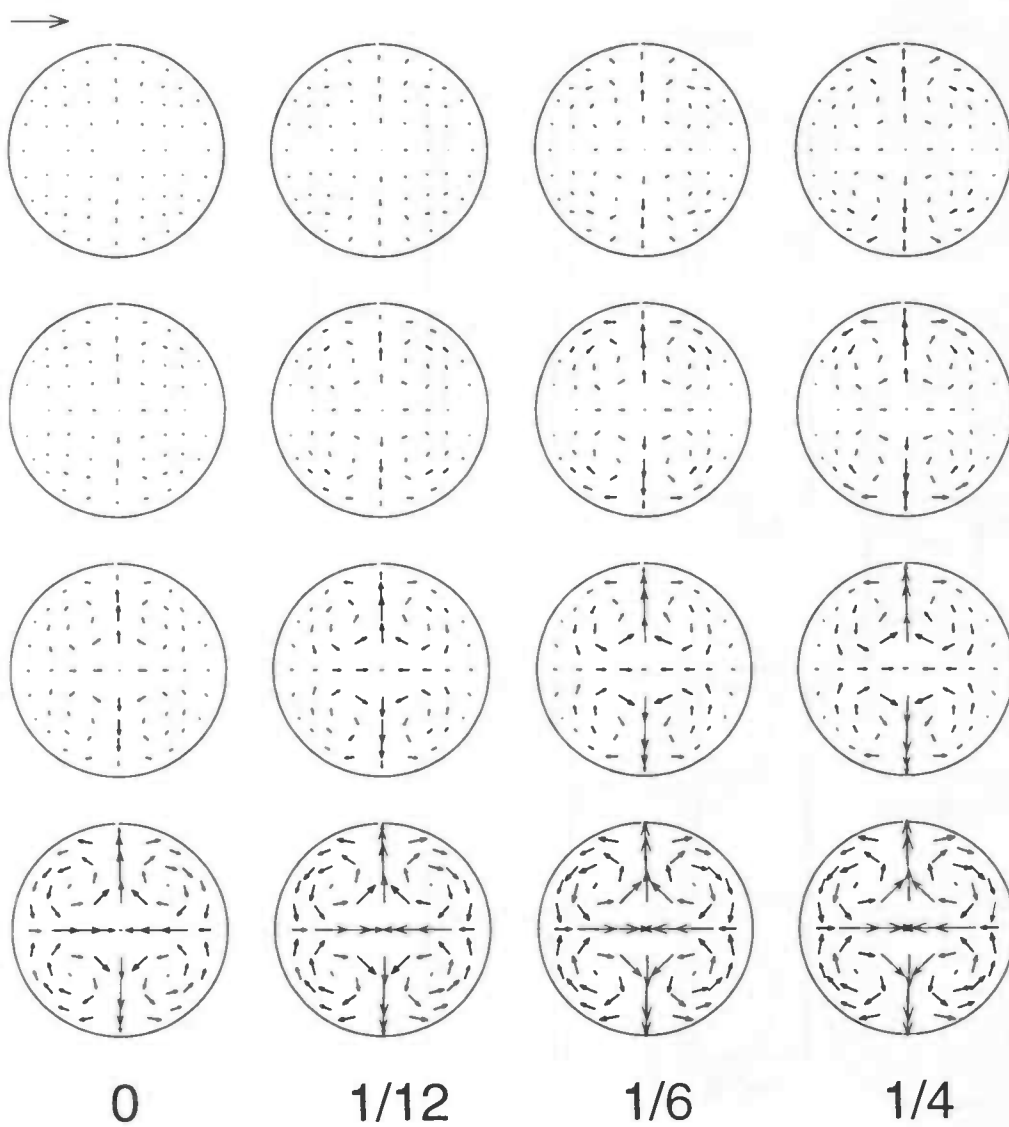


Figure 5.39: secondary velocity for $t = 0, \frac{1}{12}, \frac{1}{6}$ and $\frac{1}{4}$.

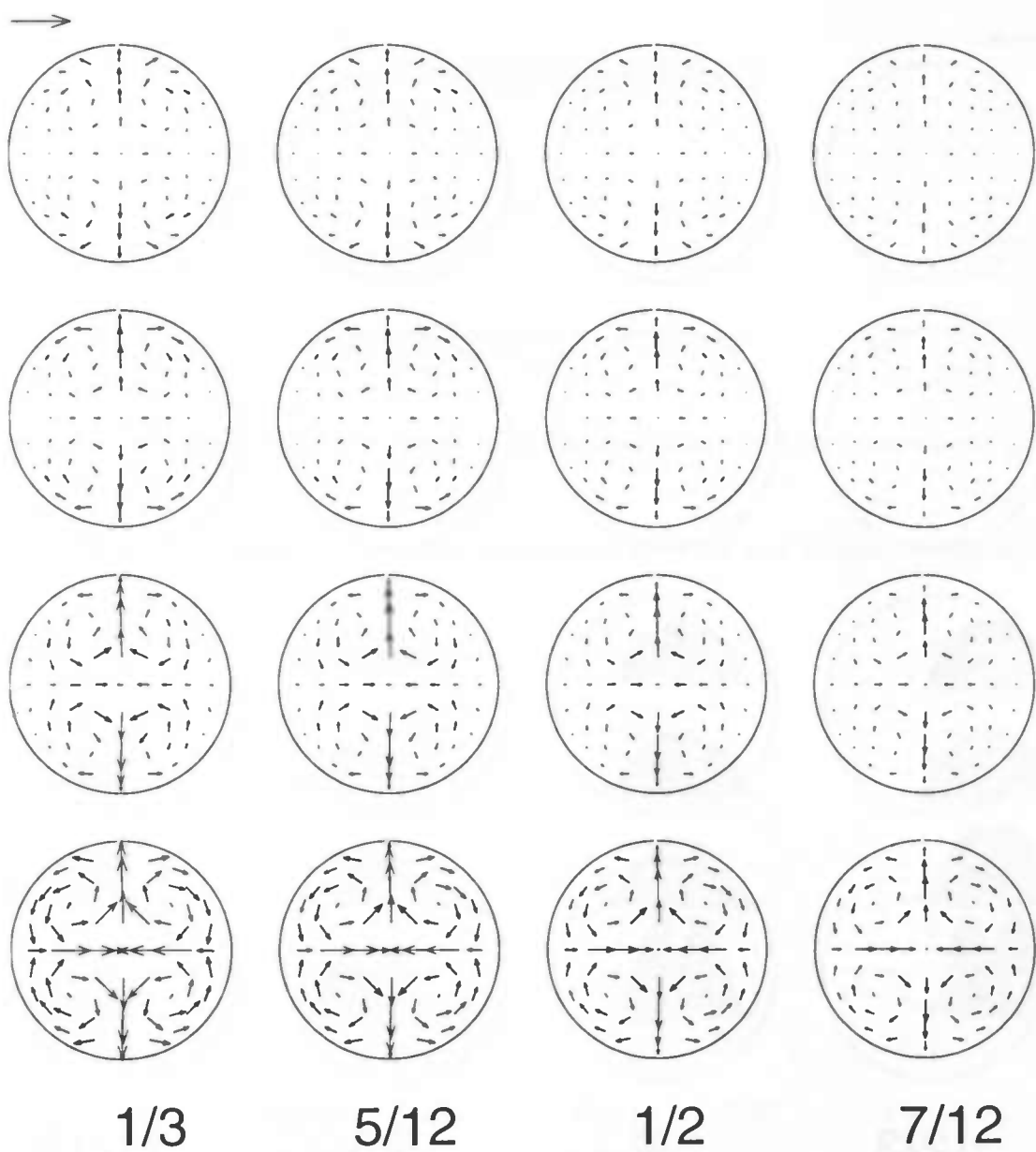


Figure 5.40: secondary velocity for $t = \frac{1}{3}, \frac{5}{12}, \frac{1}{2}$ and $\frac{7}{12}$.

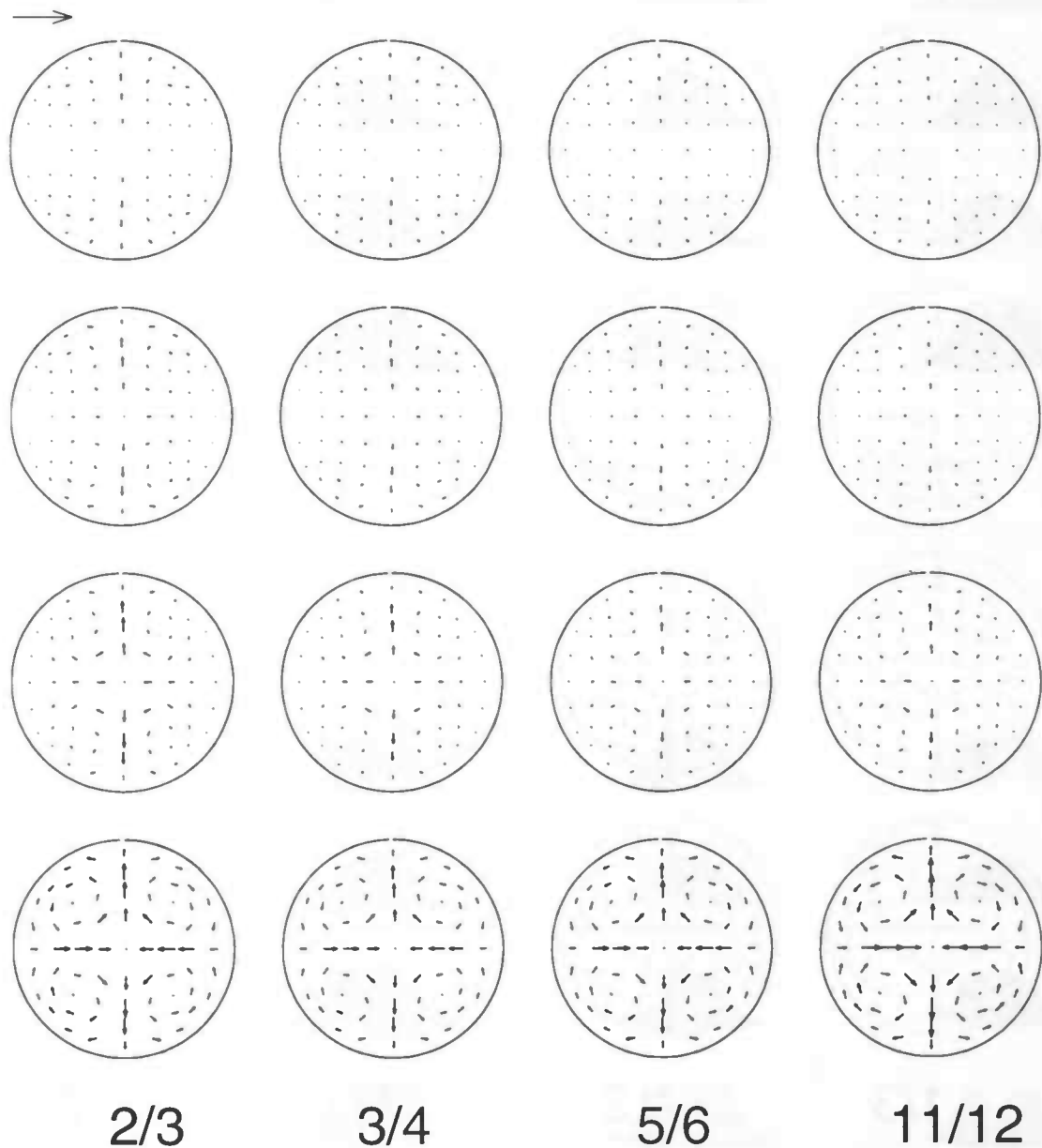


Figure 5.41: secondary velocity for $t = \frac{2}{3}, \frac{3}{4}, \frac{5}{6}$ and $\frac{11}{12}$.

In the next plots the results of the computations of a pulsating flow in the basilar artery are given. The pulse of the heart is given in figure 5.42 (see also section 4.3.3). The Reynolds number $Re = 150$. The plots are given for the following moments in time.

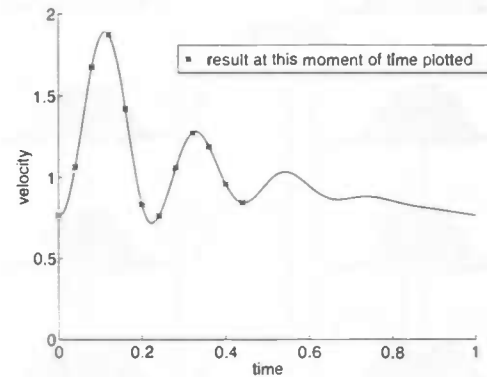


Figure 5.42: normalized puls of the heart in the basilar artery and the moments of time at which results are given

The velocity plots are made at the inflow surface and after 1,2 and 3 times the diameter.

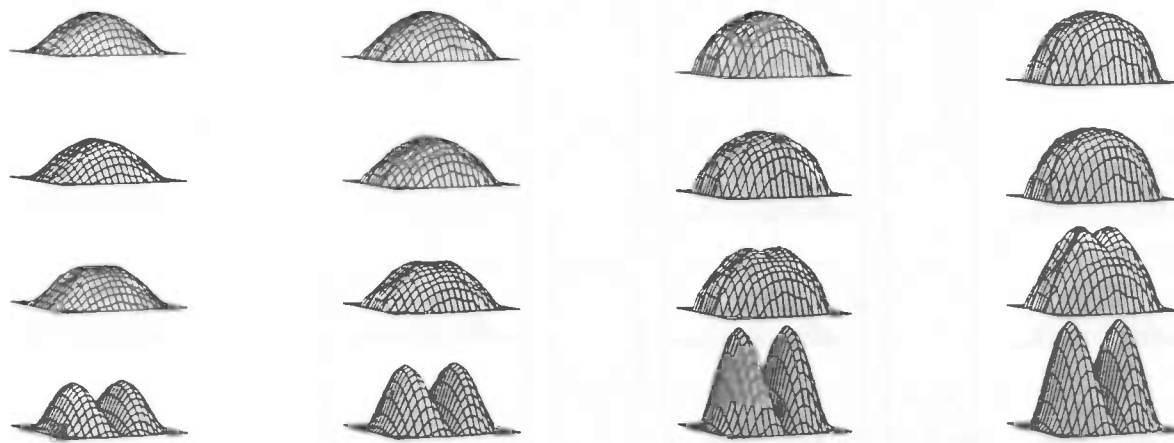


Figure 5.43: $t = 0$

Figure 5.44: $t = 0.04$

Figure 5.45: $t = 0.08$

Figure 5.46: $t = 0.12$



Figure 5.47:
 $t = 0.16$

Figure 5.48:
 $t = 0.2$

Figure 5.49:
 $t = 0.24$

Figure 5.50:
 $t = 0.28$



Figure 5.51:
 $t = 0.32$

Figure 5.52:
 $t = 0.36$

Figure 5.53:
 $t = 0.4$

Figure 5.54:
 $t = 0.44$

In the next plots the cross-sections of the velocity profiles along the x and y axes are given. The cross-sections have been made after diameter 0 till 3. On the left the results of a stationary flow are presented.

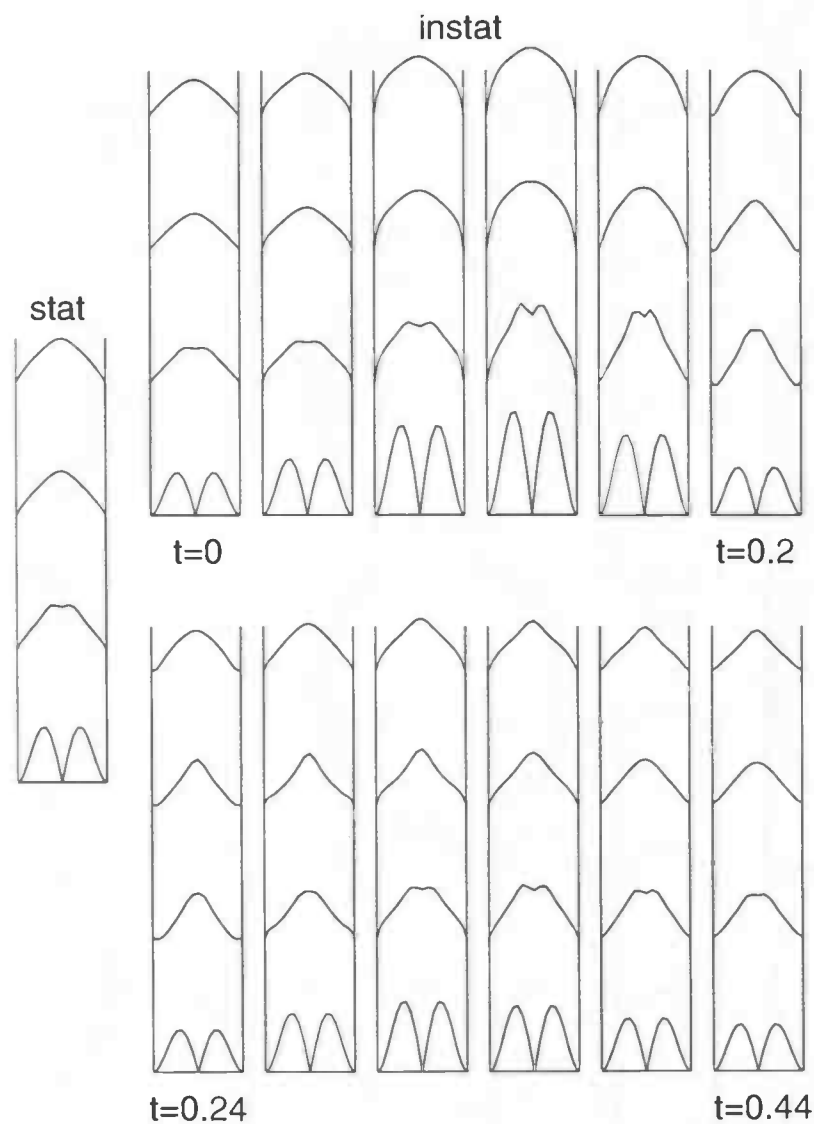


Figure 5.55: cross-section of the velocity along the x axis. $Re = 150$

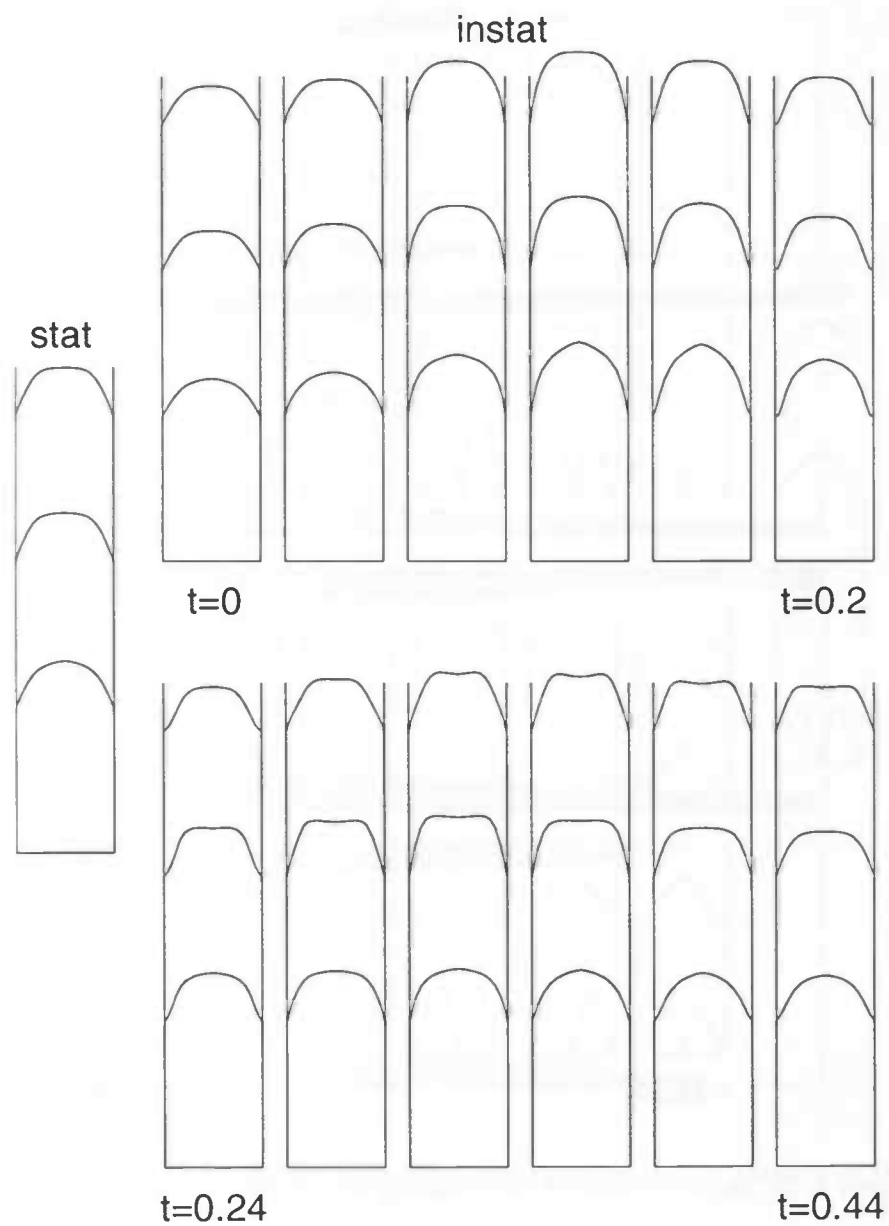


Figure 5.56: cross-section of the velocity along the y axis. $Re = 150$

In the next figures contour plots of the negative axial velocity are given. The inflow profile is pulsating and the Reynolds number $Re = 150$. The plots are given after 1,2 and 3 times the diameter and for $t = 0.18$ (below), 0.20, 0.22 and 0.24.

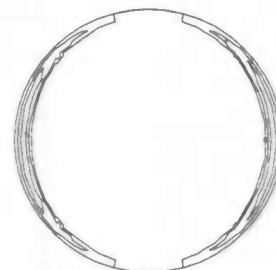
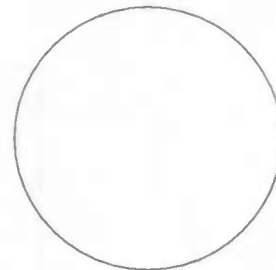
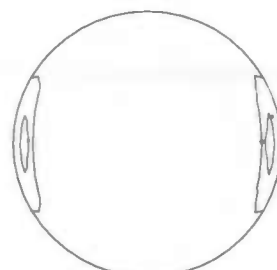
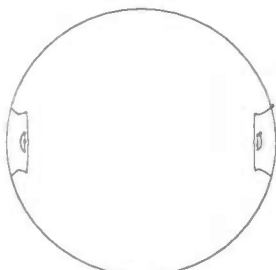


Figure 5.57: after 1 diameter

Figure 5.58: after 2 diameters

Figure 5.59: after 3 diameters

In the next plots contour plots of the negative axial velocity are given. The plots are made in the plane $y = 0$. The inflow profile is pulsating and the Reynolds number $Re = 150$. The plots are made for $t = 0.18$ till 0.24 (below).

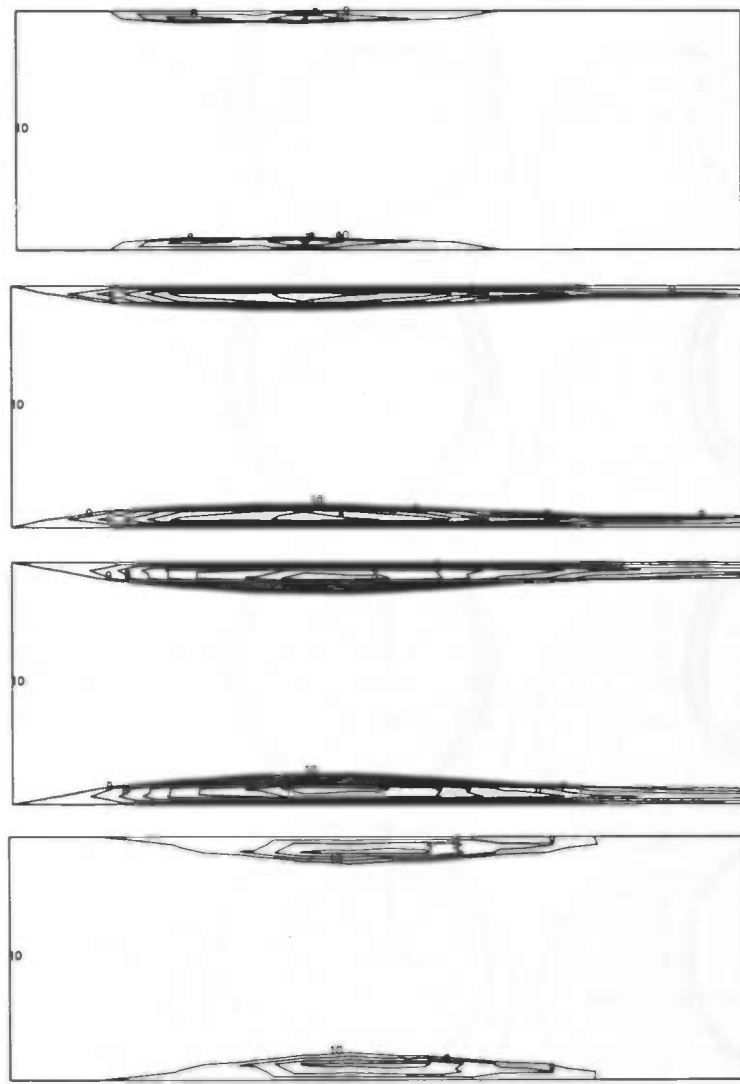


Figure 5.60: Contour plots of the negative axial velocity in the plane $y = 0$. $Re = 150$.

In the next plots the secondary velocity of the pulsating flow is given. The arrow above the plots indicates the time averaged mean axial velocity. The Reynolds number $Re = 150$.

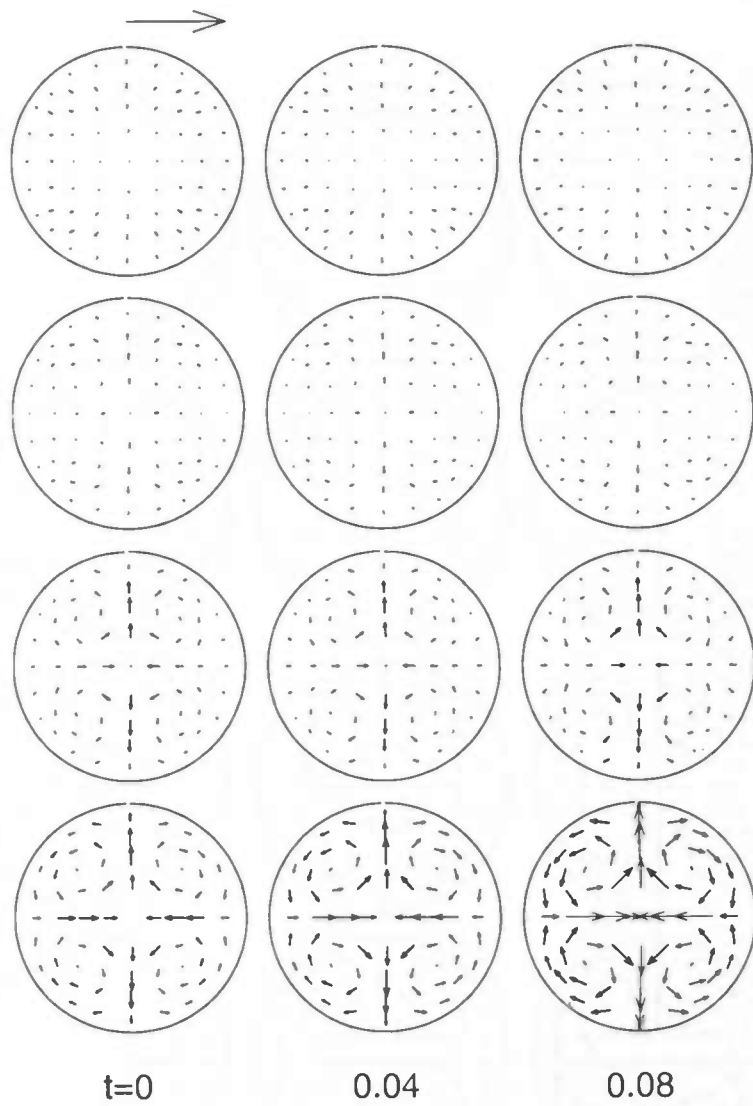


Figure 5.61: secondary velocity for $t = 0$ till 0.08

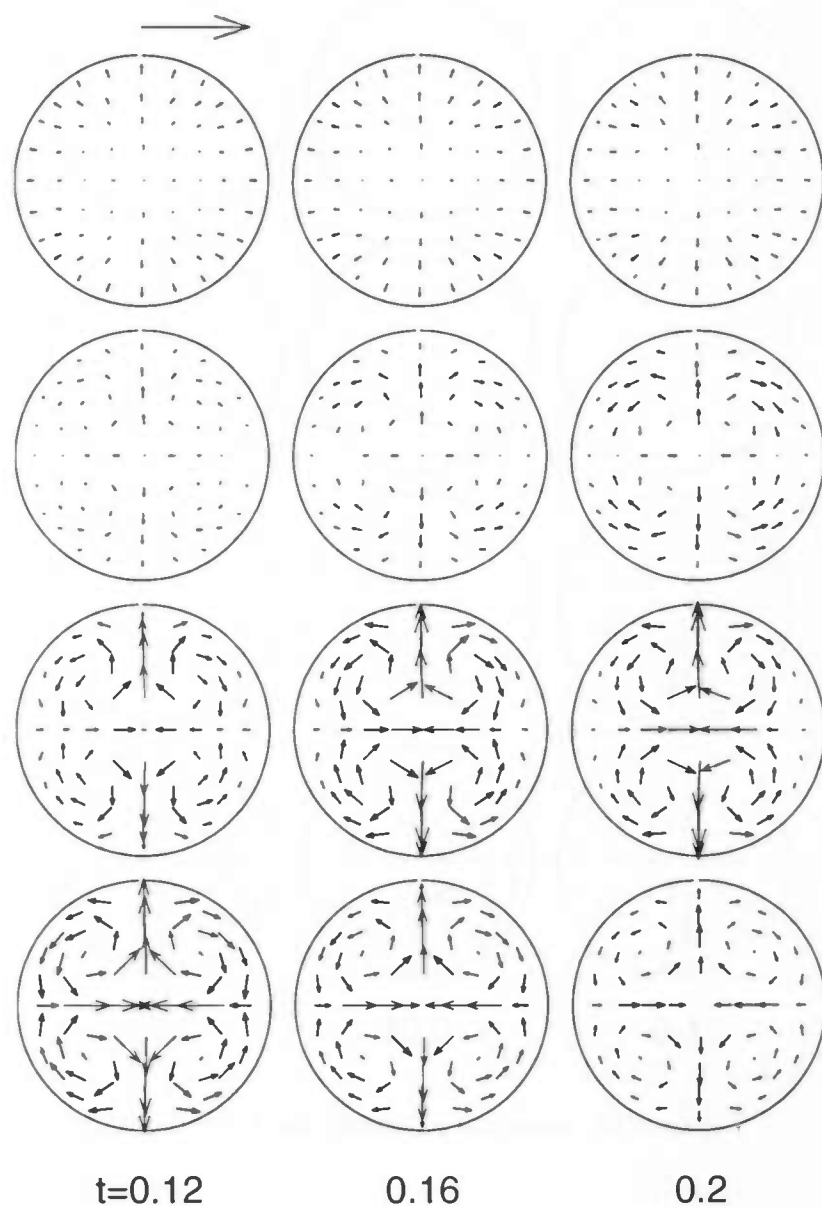


Figure 5.62: secondary velocity for $t = 0.12$ till 0.20

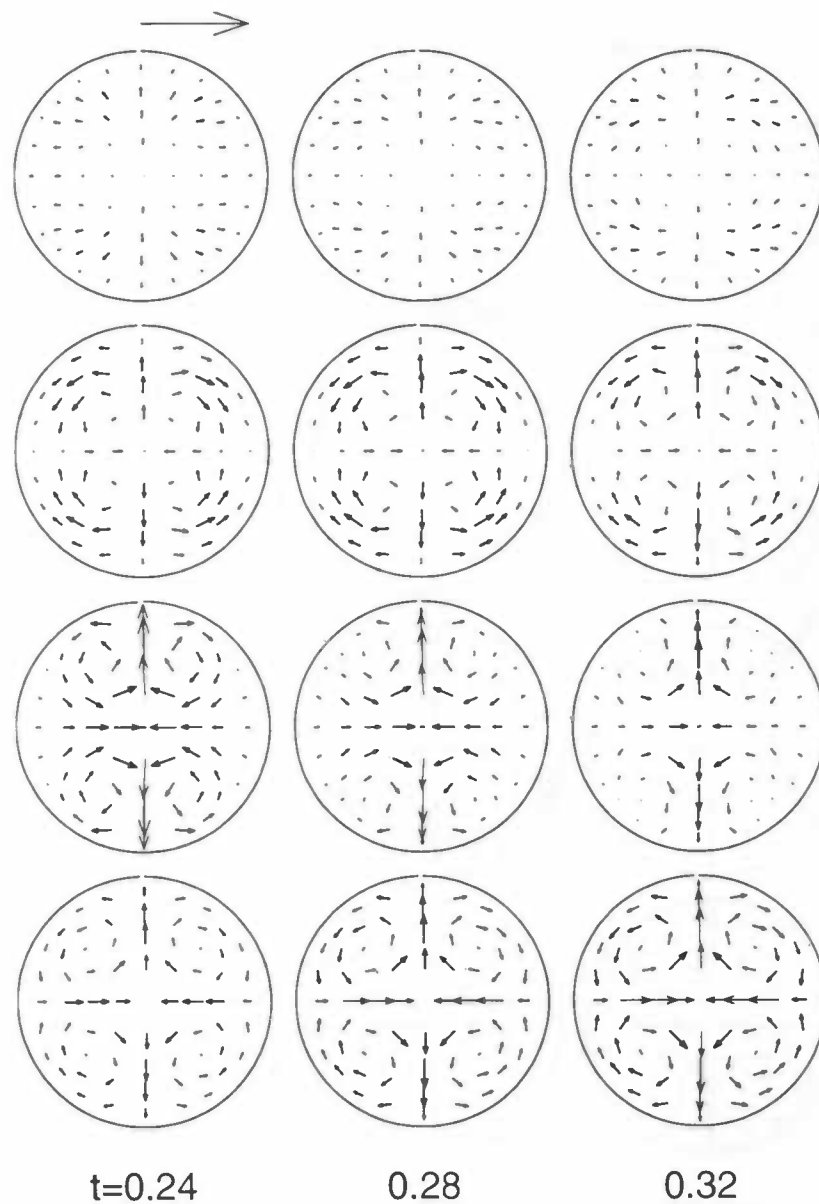


Figure 5.63: secondary velocity for $t = 0.24$ till 0.32

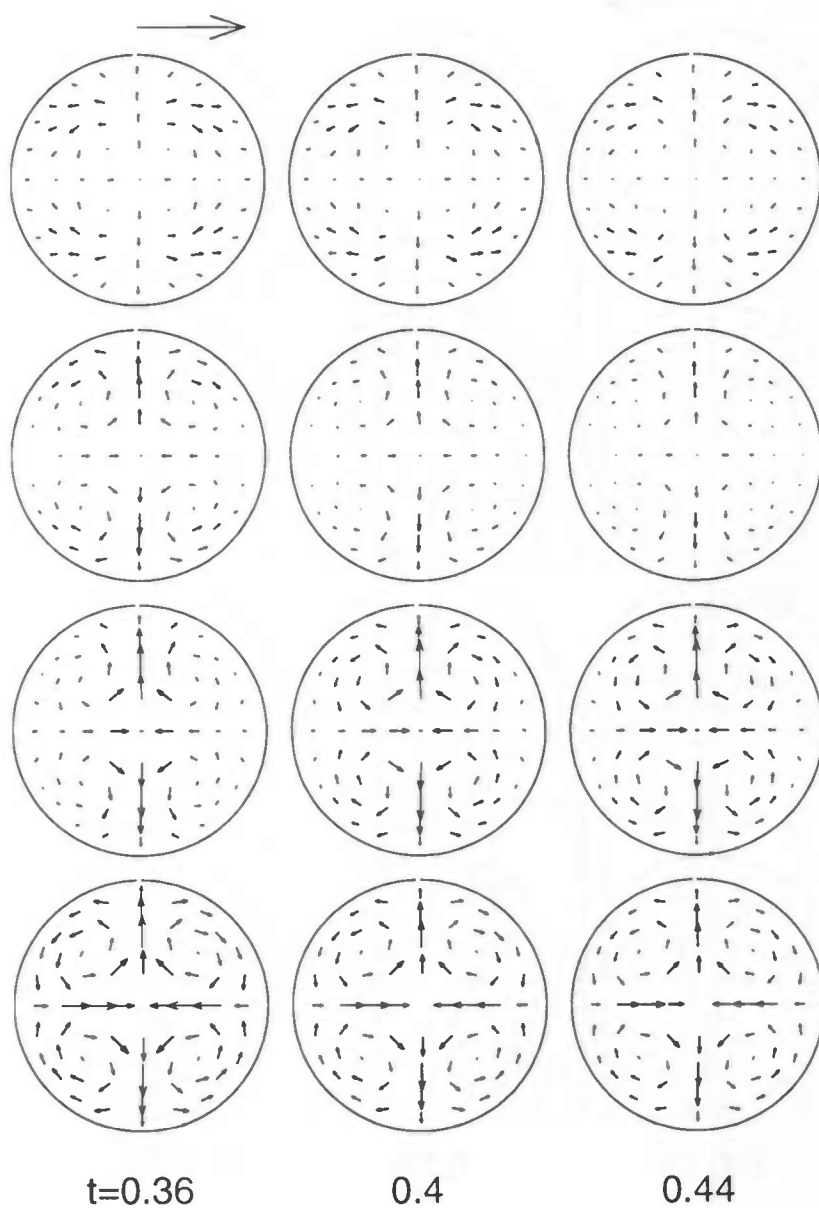


Figure 5.64: secondary velocity for $t = 0.36$ till 0.44

In the next figures contour plots of the negative axial velocity are given. The inflow profile is pulsating and the Reynolds number $Re = 150$. There is no prescribed secondary velocity field. The plots are given after 1,2 and 3 times the diameter and for $t = 0.18$ (below), 0.20, 0.22 and 0.24.

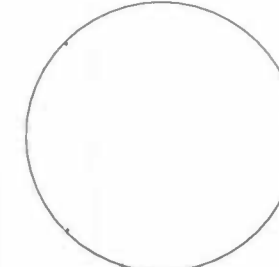
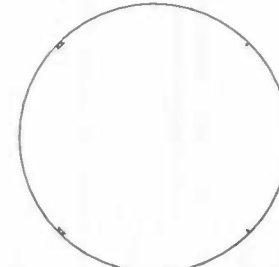
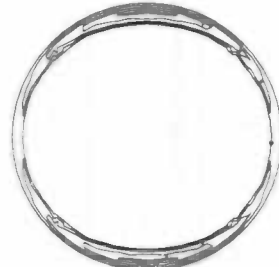
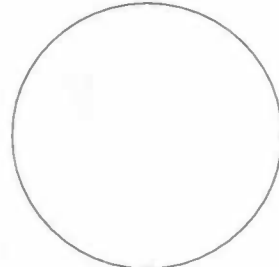
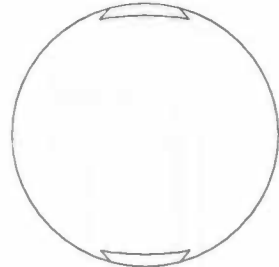
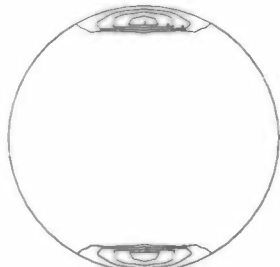


Figure 5.65: after 1 diameter

Figure 5.66: after 2 diameters

Figure 5.67: after 3 diameters

In the next plots the cross-sections of the velocity profiles along the x and y axes are given. The cross-sections have been made after diameter 0 till 3. On the left the results of a stationary flow are presented. The inflow profile is pulsating and no secondary velocity field is prescribed.

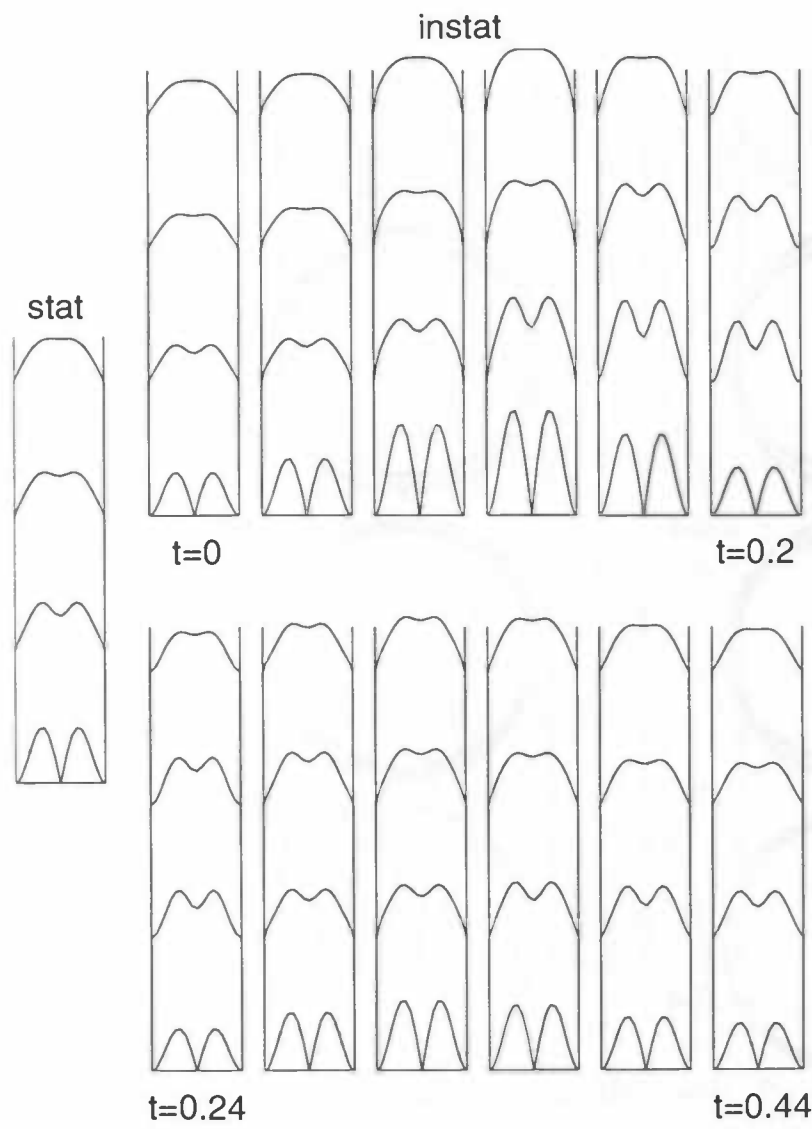


Figure 5.68: cross-section of the velocity along the x axis. $Re = 150$

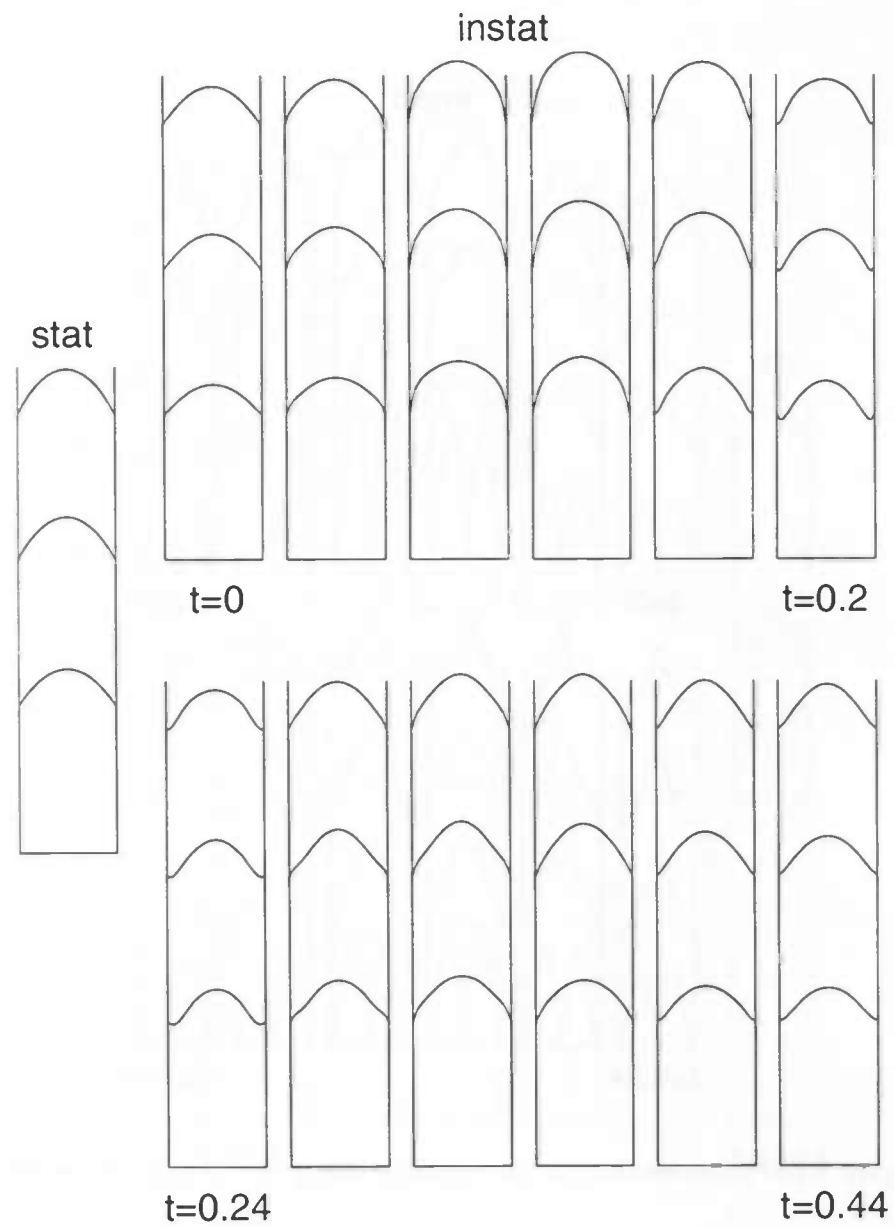


Figure 5.69: cross-section of the velocity along the y axis. $Re = 150$

In the next plots the cross-sections of the velocity profiles along the x and y axes are given. The cross-sections have been made after diameter 0 till 3. On the left the results of a stationary flow are presented. The inflow profile is pulsating and a secondary velocity field is prescribed. The Reynolds number $Re = 300$

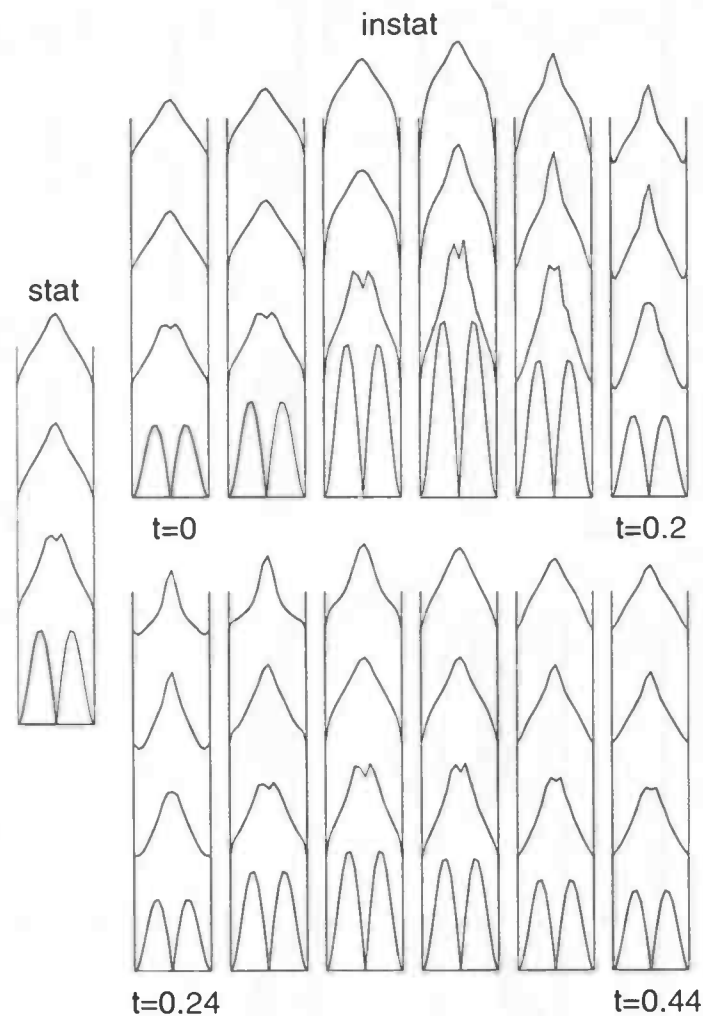


Figure 5.70: cross-section of the velocity along the x axis. $Re = 300$

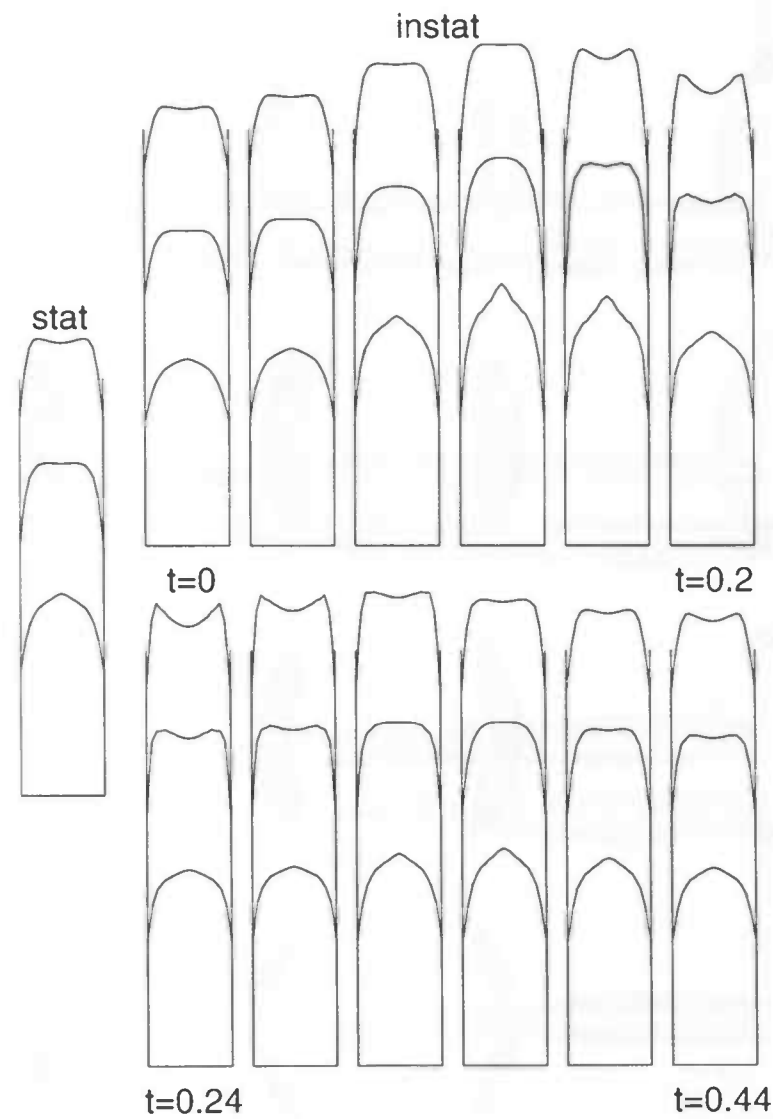


Figure 5.71: cross-section of the velocity along the y axis. $Re = 300$

In the next figures contour plots of the negative axial velocity are given. The inflow profile is pulsating and the Reynolds number $Re = 300$. A secondary velocity field is prescribed. On the left the plots are computed after 1 diameter and for $t = 0.16$ (below), 0.18, 0.20 and 0.22. In the middle and on the right the plots are computed after 2 and 3 times the diameter and for $t = 0.18$ (below), 0.20, 0.22 and 0.24.

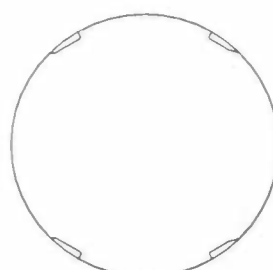
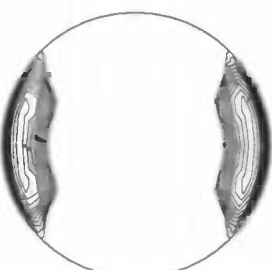
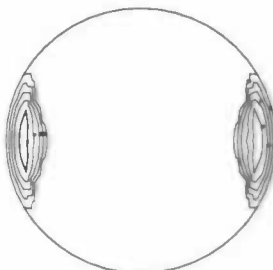
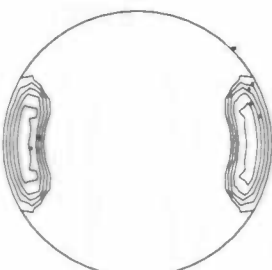


Figure 5.72: after 1 diameter

Figure 5.73: after 2 diameters

Figure 5.74: after 3 diameters

In the next plots contour plots of the negative axial velocity are given. The plots are made in the plane $y = 0$. The inflow profile is pulsating and the Reynolds number $Re = 300$. A secondary velocity field is prescribed. The plots are made for $t = 0.18$ till 0.24 (below).

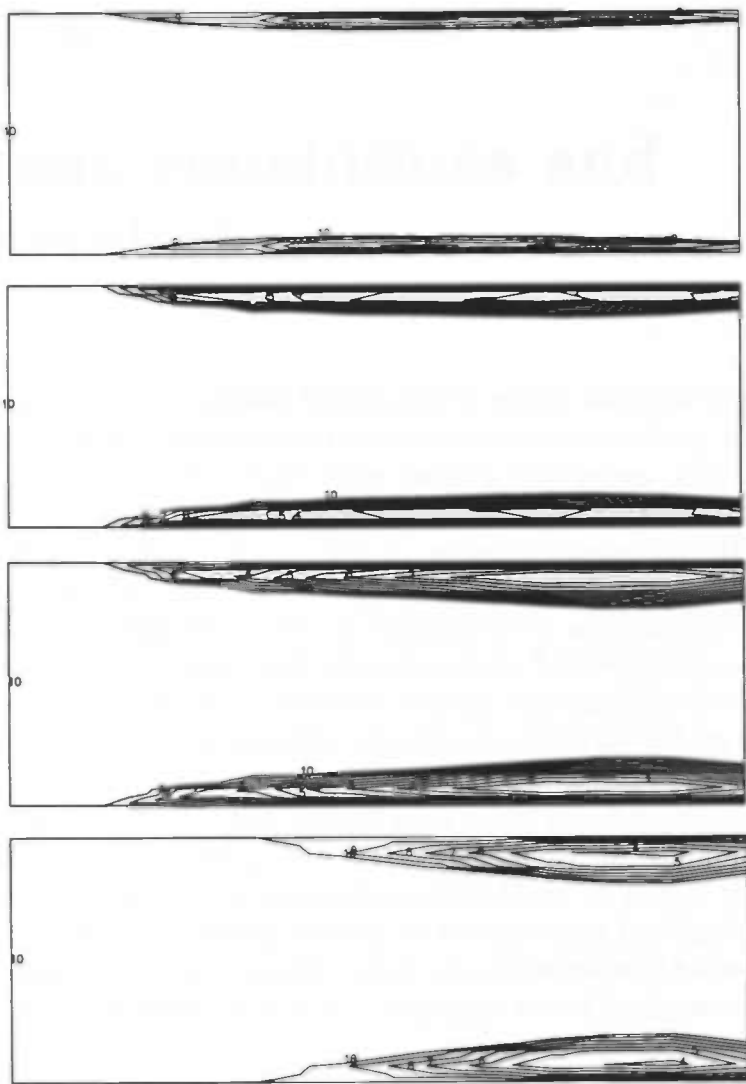


Figure 5.75: Contour plots of the negative axial velocity in the plane $y = 0$. $Re = 300$.



Chapter 6

Discussion, conclusions and recommendations

The description of a three-dimensional flow in a tube with a finite element method package as SEPRAN takes a lot of computation time and computer memory space. To solve this problem we tried to place several short tubes behind each other. This saves a lot of time and memory space. In the case of a stationary flow this principle was a good one. The error that was made, was about 0.3% (in the L_2 norm) per transition. However, in the case of an instationary flow the error was far greater, especially in the phase of acceleration. This can be concluded from the tables of differences in section 4.2. We conclude that the method to place tubes behind each other is not to be used when accurate results for instationary flows are desired. A possible solution for this problem is to compute the flow in the first tube for all time steps and after that to transpose the values to the second tube.

However, the method to place tubes behind each other is a feasible method to get some preliminary insight in the unsteady flow phenomena. On our computer CIWI10 it was not possible to obtain results for a three-dimensional flow in a tube that was sufficiently long to show the ultimate Womersley profile. It is clear from the figures on page 38 of an instationary flow that the velocity profiles show the characteristic hollow shape of velocity profiles in phase of deceleration. When the frequency would be increased, backflow might occur.

For the computations of a stationary flow with secondary velocity the results agree with the phenomena found in [9]. For a harmonically oscillating, instationary flow the results showed recirculation regions. Backflow occurs when the flow decelerates the most. These regions are the most likely to be affected with atherosclerosis. Also in the case of a pulsating entry flow backflow occurs. However, the magnitude of the backflow is far greater. This is caused by the fast acceleration and deceleration of the velocity. The backflow at the outflow plane might give a problem, because of the inflow from the "outside world", but the interior flow pattern seems to be correct. The influences of the prescribed secondary velocity are well visible when comparing the results of the computation with the

results obtained from a flow without the prescribed secondary velocity. The position of the recirculation regions is clearly affected by the secondary velocity. In the basilar artery the recirculation regions are situated along the wall in the plane formed by the bends of the vertebral arteries.

The conclusions of this report are:

- The method to compute a stationary flow in several tubes placed behind each other is a good one.
- This method can not be used for instationary flows.
- In the basilar artery a strong backflow appears.

Furthermore there are some topics for further research:

- The flow was simulated in a straight, circular tube. The secondary velocity was prescribed at the inflow plane. The simulation would be more realistic when the flow is also simulated in the last piece of the two vertebral arteries. The secondary velocity then arises automatically. It is also recommendable to experiment with a curved tube instead of a straight tube.
- The frequency of the pulse applied in this report was 60 beats per minute. When the frequency of the pulse is increased, the gradients of the velocity will be larger. In that case the magnitude of the backflow may be also larger.
- If further research is done, it will be good to use another program than SEPRAN. When computing a pulsating, three-dimensional flow SEPRAN is a very heavy and slow package. The use of COMFLO for example will give a huge reduction of computing time.

Bibliography

- [1] Atkinson, K.E. (1988)
An introduction to numerical analysis
John Wiley & Sons, Inc.
- [2] Botta, E.F.F. (1991)
De methode der Eindige Elementen
Department of Mathematics, University of Groningen
- [3] Bowman, F. (1958)
Introduction to Bessel Functions
Dover Publications Inc., New York
- [4] Cuvelier, C. et al (1986)
Finite Element Methods and the Navier-Stokes equations
D.Reidel Publishing Company
- [5] Dijkstra, E.J. (1991)
Pulsating entry-flow in a straight circular tube
Department of Mathematics, University of Groningen
- [6] Girault,V. and Raviart, P.A. (1979)
Finite element approximation of the Navier-Stokes equations
Springer
- [7] Hoogstraten, H.W. (1992)
Stromingsleer
Department of Mathematics, University of Groningen
- [8] Krijger, J.K.B., Hillen, B. and Hoogstraten, H.W. (1991)
Pulsating entry flow in a plane channel
J. Appl. Math. Phys. 42, 139-153
- [9] Ravensbergen, J. (1995)
The basilar artery: Interaction between form and flow
Ph.D. thesis, Department of Functional Anatomy, Utrecht University

- [10] Veldman, A.E.P. (1994)
Numerieke Stromingsleer
Department of Mathematics, University of Groningen
- [11] Womersley, J.R. (1955)
Method for the calculation of velocity, rate of flow and viscous drag in arteries when the pressure gradient is known
J. Physiol. 127, 553-563